



A NEW MULTI-ENERGY NEUTRINO RADIATION-HYDRODYNAMICS CODE IN FULL GENERAL RELATIVITY AND ITS APPLICATION TO THE GRAVITATIONAL COLLAPSE OF MASSIVE STARS

TAKAMI KURODA¹, TOMOYA TAKIWAKI², AND KEI KOTAKE^{3,4}¹ Department of Physics, University of Basel, Klingelbergstrasse 82, 4056 Basel, Switzerland² Astrophysical Big Bang Laboratory, RIKEN, Saitama, 351-0198, Japan³ Department of Applied Physics, Fukuoka University, 8-19-1, Jonan, Nanakuma, Fukuoka, 814-0180, Japan⁴ Division of Theoretical Astronomy, National Astronomical Observatory of Japan, 2-21-1, Osawa, Mitaka, Tokyo, 181-8588, Japan

Received 2015 January 26; accepted 2016 January 8; published 2016 February 18

ABSTRACT

We present a new multi-dimensional radiation-hydrodynamics code for massive stellar core-collapse in full general relativity (GR). Employing an M1 analytical closure scheme, we solve spectral neutrino transport of the radiation energy and momentum based on a truncated moment formalism. Regarding neutrino opacities, we take into account a baseline set in state-of-the-art simulations, in which inelastic neutrino–electron scattering, thermal neutrino production via pair annihilation, and nucleon–nucleon bremsstrahlung are included. While the Einstein field equations and the spatial advection terms in the radiation-hydrodynamics equations are evolved explicitly, the source terms due to neutrino–matter interactions and energy shift in the radiation moment equations are integrated implicitly by an iteration method. To verify our code, we first perform a series of standard radiation tests with analytical solutions that include the check of gravitational redshift and Doppler shift. A good agreement in these tests supports the reliability of the GR multi-energy neutrino transport scheme. We then conduct several test simulations of core-collapse, bounce, and shock stall of a $15M_{\odot}$ star in the Cartesian coordinates and make a detailed comparison with published results. Our code performs quite well to reproduce the results of full Boltzmann neutrino transport especially before bounce. In the postbounce phase, our code basically performs well, however, there are several differences that are most likely to come from the insufficient spatial resolution in our current 3D-GR models. For clarifying the resolution dependence and extending the code comparison in the late postbounce phase, we discuss that next-generation Exaflops class supercomputers are needed at least.

Key words: hydrodynamics – methods: numerical – neutrinos – radiation: dynamics – supernovae: general

1. INTRODUCTION

Neutrino transport is an essential ingredient for numerical simulations to clarify the theory of the core-collapse of massive stars and the formation mechanisms of compact objects (see, e.g., Janka 2012; Kotake et al. 2012b; Burrows 2013; Mezzacappa et al. 2014; Foglizzo et al. 2015 for recent reviews). In the collapsing iron core, neutrinos play crucial roles in every phase; deleptonization in the core determines the time of bounce and the mass of the proto-neutron star (PNS; e.g., Langanke et al. 2003); the gigantic internal energy trapped in the PNS is almost completely carried away by neutrinos, a tiny fraction of which contributes to the heating of the postshock material, leading to the onset of core-collapse supernovae (CCSNe) in the context of the neutrino heating mechanism (Bethe & Wilson 1985; Wilson 1985). Since these SN neutrinos are generally not in both thermal and chemical equilibrium, the distribution of neutrinos in the phase space should be computationally determined. This is a seven-dimensional (7D) problem (three-dimensional and one-dimensional (3D+1D) in spacetime and 3D in momentum space), which is why CCSN simulations are considered one of the most challenging subjects in computational astrophysics.

Primarily due to neutrino-driven convection (e.g., Bethe 1990; Herant et al. 1994; Burrows et al. 1995; Janka & Müller 1996; Müller & Janka 1997) and the standing accretion shock instability (SASI, e.g., Blondin et al. 2003; Foglizzo et al. 2006, 2007, 2012; Ohnishi et al. 2006; Blondin & Mezzacappa 2007; Iwakami et al. 2008, 2009; Fernández & Thompson 2009; Guilet & Foglizzo 2012; Hanke et al. 2012; Couch 2013;

Fernández et al. 2014), the postbounce cores are essentially of multi-dimensional (multi-D) nature.⁵ Due to the high compactness of the PNS, these multi-D fluid motions are all under the influence of the general relativistic (GR) gravity, the consideration of which used to be standard in the pioneering era of CCSN simulations (e.g., May & White 1966; Schwartz 1967). In rapidly rotating supernova cores (e.g., Woosley & Bloom 2006), magnetohydrodynamics (MHD) instabilities naturally make the core dynamics intrinsically non-spherical (e.g., Ardeljan et al. 2000; Kotake et al. 2004, 2006b; Obergaulinger et al. 2006, 2014; Burrows et al. 2007; Masada et al. 2012, 2015; Sawai et al. 2013; Iwakami et al. 2014; Nakamura et al. 2014a). All in all, in order to have the final word on the CCSN mechanisms quantitatively, one needs to deal with the 7D Boltzmann neutrino transport simulations in full GR MHD. Unfortunately, however, this still remains computationally very demanding even using exa-scale computing platforms in the next decade(s) to come (see discussions in Kotake et al. 2012a).⁶

Since the late 1990s, the ultimate spherically symmetric (1D) simulations where the GR Boltzmann transport is coupled to 1D-GR hydrodynamics have been made feasible by Liebendörfer et al. (2001) and Sumiyoshi et al. (2005; see

⁵ Recently, multi-dimensionalities in the precollapse core (e.g., Meakin et al. 2011) are also attracting much attention (e.g., Couch & Ott 2013; Müller & Janka 2015).

⁶ We here mean the feasibility of 7D-GR Boltzmann neutrino transport simulation following ~ 1 s after bounce with sufficient numerical resolutions in both space and momentum space.

Mezzacappa & Matzner 1989; Mezzacappa & Bruenn 1993a, 1993b, 1993c; Yamada 1997; Yamada et al. 1999; Bruenn et al. 2001; Liebendörfer et al. 2001, 2004 for the code developments). Unfortunately, however, these full-fledged 1D simulations fail to produce explosions except for super-AGB stars at the low-mass end (Kitaura et al. 2006). In the context of the full Boltzmann calculations, Livne et al. (2004) were the first to perform two-dimensional (2D) multi-angle (i.e., assuming axisymmetry in both space and momentum space) neutrino hydrodynamics simulations using the discrete ordinate (S_n) method. Then it was demonstrated by Ott et al. (2008) that the multi-angle transport is really important especially when the neutrino radiation field deviates significantly from spherical symmetry such as in the rapidly rotating cores (see also Brandt et al. 2011). Going beyond the assumption of axisymmetry in the multi-angle transport, Sumiyoshi & Yamada (2012) were the first to develop the fully multi-angle Boltzmann transport code and then apply it for static backgrounds (Sumiyoshi et al. 2015). More recently, Nagakura et al. (2014) extended the code to include special relativistic (SR) corrections and showed the ability of the code by performing 1D core-collapse simulation of a $15M_\odot$ model. Albeit not yet implemented in hydrodynamics simulations, several novel formulations and schemes of the full Boltzmann equation have recently been reported in Cardall et al. (2013a, 2013b), Shibata et al. (2014), and Peres et al. (2014).

At present, direct discretization of the Boltzmann transport equation fully into the neutrino angle and energy (such as by the S_n method mentioned above) is still computationally very expensive. An approximation often made in previous works is to remove the full angular dependence of the Boltzmann equation by expanding the neutrino distribution function as a series of moments. The simplest version, in which one closes the moment expansion after the zeroth angular moment, is the multi-group, flux-limited diffusion (MGFLD) scheme (e.g., Bruenn 1985; Livne et al. 2004; Kotake et al. 2006a; Swesty & Myra 2009; Bruenn et al. 2013; Zhang et al. 2013). In FLD schemes, the basic equation is a diffusion equation for the neutrino energy density. In solving it, an appropriate flux-limiter should be employed (e.g., Minerbo 1978; Pomraning 1981; Levermore 1984; Janka 1992) to ensure the causality of the radiation field in the transparent regions where the diffusion approximation breaks down. The isotropic diffusion source approximation (IDSA) scheme developed by Liebendörfer et al. (2009) is basically positioned at a similar approximation level compared to the MGFLD scheme. In the IDSA, the neutrino distribution function is divided into two components, one which is trapped with matter and has isotropic distribution function and the other in the free streaming limit, each of which is solved independently, while satisfying the 1D Boltzmann equation as a whole. Due to the high computational efficiency, the IDSA has been extensively employed in both 2D (Suwa et al. 2010, 2011, 2013, 2016; Nakamura et al. 2014b) and 3D simulations (Takiwaki et al. 2012, 2014). One can also truncate the angular moment at the second order and transport the zeroth and first order angular moments. In this case, higher or equal to the second order moment needs to be determined independently to close the set of transport equations. In the M1 moment scheme (e.g., Pons et al. 2000; Shibata et al. 2011), one applies an analytic formula for the closure relation (see examples applied in post-Newtonian MHD simulations (Obergauger et al. 2014) and GR simulations in 1D (O’Connor &

Ott 2013; O’Connor 2015) and in 3D (Kuroda et al. 2012, 2014). In contrast, one can self-consistently determine the closure relation by the variable Eddington factor (VEF) method (e.g., Müller et al. 2010 and see references therein). In these cases, a model Boltzmann equation is integrated to iteratively obtain the solution up to the higher moments (i.e., the Eddington tensor) until the system is converged. Currently, the multi-D state-of-the-art simulations of CCSNe are defined by multi-group (spectral) neutrino hydrodynamics simulations. More severe approximations include gray transport (Fryer et al. 1999; Scheck et al. 2006) or the light bulb and leakage schemes (e.g., Janka & Müller 1996; Ruffert et al. 1996; Kotake et al. 2003; Rosswog & Liebendörfer 2003; Murphy & Burrows 2008; O’Connor & Ott 2011; Perego et al. 2014), which have been often employed in many recent studies of multi-D instabilities and the MHD mechanism of CCSNe.

In addition to the multi-D and multi-angle/truncated neutrino transport, the accurate treatment of GR is highly ranked among the to do lists toward the ultimate CCSN simulations. In most previous multi-D models with multi-group neutrino transport, attempts to model GR effects have been made by using a modified gravitational potential that takes into account a 1D-GR effect by replacing the monopole term of Newtonian gravity with the TOV potential (Buras et al. 2006a, 2006b; Bruenn et al. 2009; Marek & Janka 2009; Hanke et al. 2013). While there are a number of GR core-collapse simulations in 2D (e.g., Dimmelmeier et al. 2002; Shibata & Sekiguchi 2004; Müller et al. 2012b) and in 3D (e.g., Shibata & Sekiguchi 2005; Kuroda et al. 2012, 2014; Ott et al. 2012; Mösta et al. 2014), many of them, especially in 3D, have been made, for the sake of computational cost, to employ a simplified microphysics such as by the Y_e parametrization scheme (Liebendörfer et al. 2005) or by the neutrino leakage scheme (Sekiguchi 2010). In our previous study (Kuroda et al. 2012), we performed 3D-GR/SR hydrodynamics simulations of a $15M_\odot$ star with the gray M1 scheme. We demonstrated that due to the deeper gravitational well of GR, the neutrino luminosity and the average neutrino energy in the postbounce phase increase when switching from SR to GR hydrodynamics. Since the neutrino heating rates in the postshock regions are sensitively affected by the emergent neutrino spectra, whether or not the GR effect will help the onset of neutrino-driven explosions needs to be investigated by multi-D GR simulations with a more sophisticated neutrino transport scheme.⁷

In this paper, we present a new 3D-GR radiation-hydrodynamics code that is meant to apply for stellar core-collapse simulations. The spacetime treatment is based on the Arnowitt–Deser–Misner 3+1 formalism and we employ the Baumgarte–Shapiro–Shibata–Nakamura (BSSN) formalism (Shibata & Nakamura 1995; Baumgarte & Shapiro 1999) to evolve the metric variables. The full GR radiation-hydrodynamics equations are evolved in a conservative form, in which we solve the energy-dependent set of radiation moments up to the first order with the M1 moment scheme. This part is based on the partial implementation of the Thorne’s moment

⁷ It is worth mentioning that 2D-GR models with the VEF method tend to explode more easily than the corresponding 2D Newtonian models with and without the GR correction (e.g., Müller et al. 2010, 2012b; Müller & Janka 2014). This may support the speculation that GR is helpful for the workings of the neutrino mechanism in multi-D simulations.

formalism (Thorne 1981), which is extended by Shibata et al. (2011) in a more suitable manner applicable to the neutrino transport problem. Regarding the neutrino–matter interaction terms, we employ a baseline set of weak interactions as given in Bruenn (1985) and Rampp & Janka (2002), where nucleon–nucleon bremsstrahlung is additionally taken into account. Our newly developed code is designed to evolve the Einstein field equation together with the GR radiation hydrodynamic equations in a self-consistent manner while satisfying the Hamiltonian and momentum constraints. A nested structure embedded in the 3D Cartesian computational domain enables us to follow the dynamics starting from the onset of gravitational collapse of a $15 M_{\odot}$ star (Woosley & Weaver 1995), through bounce, up to about ~ 50 ms postbounce. Since, it is still computationally too expensive to follow long-term evolution in full 3D until the neutrino-driven explosion takes place (e.g., at the earliest ~ 200 ms after bounce (Bruenn et al. 2009; Marek & Janka 2009) or ~ 500 ms in 2D-GR calculation (Müller & Janka 2014)), we mainly focus on detailed comparisons between our pseudo-1D neutrino profiles computed in the 3D Cartesian coordinates and previous 1D results to check the validity of our new code in the early postbounce phase.

This paper is organized as follows. In Section 2, after we shortly introduce the formulation of the GR transport scheme, we describe the governing equations of hydrodynamics and neutrino transport in detail. Some practical implementation schemes how to satisfy important conservative quantities such as lepton number, energy, and momentum are given in Section 3. The main results and detailed comparisons with previous studies are presented in Section 5. Note that geometrized unit system is used in Sections 2 and 3, i.e., the speed of light, the gravitational constant and the Planck constant are set to unity: $c = G = h = 1$, and cgs units are used in Section 5. Greek indices run from 0 to 3 and Latin indices from 1 to 3.

2. FORMALISM

This section starts with a brief summary of the basic equations and the numerical schemes of GR radiation hydrodynamics.

Following our previous work (Kuroda et al. 2012), our code consists of the following three parts, where the evolution equations of metric, hydrodynamics, and neutrino radiation are solved. Each of them is solved in an operator-splitting manner, but the system evolves self-consistently as a whole, satisfying the Hamiltonian and momentum constraints. Regarding the metric evolution, the spatial metric γ_{ij} (in the standard (3 + 1) form: $ds^2 = -\alpha^2 dt^2 + \gamma_{ij}(dx^i + \beta^i dt)(dx^j + \beta^j dt)$, with α and β^i being the lapse and shift, respectively) and its extrinsic curvature K_{ij} are evolved using the BSSN formulation (Shibata & Nakamura 1995; Baumgarte & Shapiro 1999; see Kuroda et al. 2012, 2014 for more details).

2.1. Radiation Hydrodynamics

There are major differences compared to our previous code (Kuroda et al. 2012). On the one hand, we evolved an energy-integrated (“gray”) neutrino radiation field with an approximate description of neutrino–matter interaction based on the neutrino leakage scheme, and on the other hand we now solve the spectral neutrino transport where the source terms are treated self-consistently following a standard procedure of the M1

closure scheme (Shibata et al. 2011). For convenience, we briefly summarize the basic equations of our newly developed code in the following (see Shibata et al. 2011 and Cardall et al. 2013a for the complete derivation).

The total stress–energy tensor $T_{(\text{total})}^{\alpha\beta}$ is expressed as

$$T_{(\text{total})}^{\alpha\beta} = T_{(\text{fluid})}^{\alpha\beta} + \int d\varepsilon \sum_{\nu \in \nu_e, \bar{\nu}_e, \nu_x} T_{(\nu, \varepsilon)}^{\alpha\beta}, \quad (1)$$

where $T_{(\text{fluid})}^{\alpha\beta}$ and $T_{(\nu, \varepsilon)}^{\alpha\beta}$ are the stress–energy tensor of fluid and the energy-dependent neutrino radiation field, respectively. Note in the above equation, summation is taken for all species of neutrinos ($\nu_e, \bar{\nu}_e, \nu_x$) with ν_x representing heavy lepton neutrinos (i.e., ν_{μ}, ν_{τ} and their anti-particles), and ε represents neutrino energy measured in the comoving frame with the fluid. For simplicity, the neutrino flavor index ν is omitted below.

With introducing radiation energy ($E_{(\varepsilon)}$), radiation flux ($F_{(\varepsilon)}^{\mu}$), and radiation pressure ($P_{(\varepsilon)}^{\mu\nu}$), measured by an Eulerian observer or ($J_{(\varepsilon)}, H_{(\varepsilon)}^{\mu}$ and $L_{(\varepsilon)}^{\mu\nu}$) measured in a comoving frame, $T_{(\varepsilon)}^{\mu\nu}$ can be written in covariant form as

$$T_{(\varepsilon)}^{\mu\nu} = E_{(\varepsilon)} n^{\mu} n^{\nu} + F_{(\varepsilon)}^{\mu} n^{\nu} + F_{(\varepsilon)}^{\nu} n^{\mu} + P_{(\varepsilon)}^{\mu\nu}, \quad (2)$$

$$= J_{(\varepsilon)} u^{\mu} u^{\nu} + H_{(\varepsilon)}^{\mu} u^{\nu} + H_{(\varepsilon)}^{\nu} u^{\mu} + L_{(\varepsilon)}^{\mu\nu}. \quad (3)$$

In the above equations, $n^{\mu} = (1/\alpha, -\beta^k/\alpha)$ is a unit vector orthogonal to the space-like hypersurface and u^{μ} is the four velocity of fluid. In the truncated moment formalism (Thorne 1981; Shibata et al. 2011), one evolves radiation energy ($E_{(\varepsilon)}$) and radiation flux ($F_{(\varepsilon)}^{\alpha}$) in a conservative form and $P_{(\varepsilon)}^{\mu\nu}$ is determined by an analytic closure relation (e.g., Equation (6)). The evolution equations for $E_{(\varepsilon)}$ and $F_{(\varepsilon)}^{\alpha}$ are given by

$$\begin{aligned} & \partial_t \sqrt{\gamma} E_{(\varepsilon)} + \partial_i \sqrt{\gamma} (\alpha F_{(\varepsilon)}^i - \beta^i E_{(\varepsilon)}) + \sqrt{\gamma} \alpha \partial_{\varepsilon} (\varepsilon \tilde{M}_{(\varepsilon)}^{\mu} n_{\mu}) \\ & = \sqrt{\gamma} (\alpha P_{(\varepsilon)}^{ij} K_{ij} - F_{(\varepsilon)}^i \partial_i \alpha - \alpha S_{(\varepsilon)}^{\mu} n_{\mu}), \end{aligned} \quad (4)$$

and

$$\begin{aligned} & \partial_t \sqrt{\gamma} F_{(\varepsilon)i} + \partial_j \sqrt{\gamma} (\alpha P_{(\varepsilon)i}^j - \beta^j F_{(\varepsilon)i}) - \sqrt{\gamma} \alpha \partial_{\varepsilon} (\varepsilon \tilde{M}_{(\varepsilon)}^{\mu} \gamma_{i\mu}) \\ & = \sqrt{\gamma} [-E_{(\varepsilon)} \partial_i \alpha + F_{(\varepsilon)j} \partial_i \beta^j + (\alpha/2) P_{(\varepsilon)}^{jk} \partial_i \gamma_{jk} + \alpha S_{(\varepsilon)}^{\mu} \gamma_{i\mu}], \end{aligned} \quad (5)$$

respectively. Here γ is the determinant of the three metric $\gamma \equiv \det(\gamma_{ij})$ and $S_{(\varepsilon)}^{\mu}$ is the source term for neutrino matter interactions (see Appendix A for the currently implemented processes). $\tilde{M}_{(\varepsilon)}^{\mu}$ is defined by $\tilde{M}_{(\varepsilon)}^{\mu} \equiv M_{(\varepsilon)}^{\mu\alpha\beta} \nabla_{\beta} u_{\alpha}$, where $M_{(\varepsilon)}^{\mu\alpha\beta}$ denotes the third rank moment of the neutrino distribution function (see Shibata et al. 2011 for the explicit expression).

By adopting the M1 closure scheme, the radiation pressure can be expressed as

$$P_{(\varepsilon)}^{ij} = \frac{3\chi_{(\varepsilon)} - 1}{2} P_{(\text{thin}(\varepsilon))}^{ij} + \frac{3(1 - \chi_{(\varepsilon)})}{2} P_{(\text{thick}(\varepsilon))}^{ij}, \quad (6)$$

where $\chi_{(\varepsilon)}$ represents the variable Eddington factor, and $P_{(\text{thin}(\varepsilon))}^{ij}$ and $P_{(\text{thick}(\varepsilon))}^{ij}$ correspond to the radiation pressure in the optically thin and thick limit, respectively. They are written in terms of $J_{(\varepsilon)}$ and $H_{(\varepsilon)}^{\mu}$ (Shibata et al. 2011). Following Minerbo (1978), Cernohorsky & Bludman (1994), and Obergaulinger & Janka

(2011), we take the variable Eddington factor $\chi_{(\varepsilon)}$ as

$$\chi_{(\varepsilon)} = \frac{5 + 6\bar{F}_{(\varepsilon)}^2 - 2\bar{F}_{(\varepsilon)}^3 + 6\bar{F}_{(\varepsilon)}^4}{15}, \quad (7)$$

where

$$\bar{F}_{(\varepsilon)}^2 \equiv \frac{h_{\mu\nu} H_{(\varepsilon)}^\mu H_{(\varepsilon)}^\nu}{J_{(\varepsilon)}^2}. \quad (8)$$

In Equation (8), $h_{\mu\nu} \equiv g_{\mu\nu} + u_\mu u_\nu$ is the projection operator. As we will discuss later, by the definition of $\bar{F}_{(\varepsilon)}$ in Equation (8), one can appropriately reproduce several important neutrino behaviors, for example, neutrino trapping in the rapidly collapsing opaque core. We iteratively solve the simultaneous Equations (7)–(8) to find the converged solution of $\chi_{(\varepsilon)}$.

The hydrodynamic equations are written in a conservative form as

$$\partial_t \rho_* + \partial_i (\rho_* v^i) = 0, \quad (9)$$

$$\begin{aligned} & \partial_t \sqrt{\gamma} S_i + \partial_j \sqrt{\gamma} (S_i v^j + \alpha P \delta_i^j) \\ &= -\sqrt{\gamma} [S_0 \partial_i \alpha - S_k \partial_i \beta^k - 2\alpha S_k^k \partial_i \phi \\ &+ \alpha e^{-4\phi} (S_{jk} - P \gamma_{jk}) \partial_i \tilde{\gamma}^{jk} / 2 + \alpha \int d\varepsilon S_{(\varepsilon)}^\mu \gamma_{i\mu}], \end{aligned} \quad (10)$$

$$\begin{aligned} & \partial_t \sqrt{\gamma} \tau + \partial_i \sqrt{\gamma} (\tau v^i + P(v^i + \beta^i)) \\ &= \sqrt{\gamma} [\alpha K S_k^k / 3 + \alpha e^{-4\phi} (S_{ij} - P \gamma_{ij}) \tilde{A}^{ij} \\ &- S_i D^i \alpha + \alpha \int d\varepsilon S_{(\varepsilon)}^\mu n_\mu], \end{aligned} \quad (11)$$

$$\partial_t (\rho_* Y_e) + \partial_i (\rho_* Y_e v^i) = \sqrt{\gamma} \alpha m_u \int \frac{d\varepsilon}{\varepsilon} (S_{(\nu_e, \varepsilon)}^\mu - S_{(\bar{\nu}_e, \varepsilon)}^\mu) u_\mu, \quad (12)$$

where $\rho_* = \rho \sqrt{\gamma} W$, $S_i = \rho h W u_i$, $S_{ij} = \rho h u_i u_j + P \gamma_{ij}$, $S_k^k = \gamma^{ij} S_{ij}$, $S_0 = \rho h W^2 - P$, and $\phi = \log(\gamma)/12$. ρ is the rest mass density, W is the Lorentz factor, $h = 1 + e + P/\rho$ is the specific enthalpy, $v^i = u^i/u^t$, $\tau = S_0 - \rho W$, $Y_e \equiv n_e/n_b$ is the electron fraction (n_X is the number density of X), e and P are the specific internal energy and pressure of matter, respectively, and m_u is the atomic mass unit. $P(\rho, s, Y_e)$ and $e(\rho, s, Y_e)$ are given by an equation of state (EOS) with s denoting the entropy per baryon. We employ an EOS by Lattimer & Douglas Swesty (1991, hereafter LS220; see Section 5.1 for more details). In the right-hand side (rhs) of Equation (11), D^i represents the covariant derivative with respect to the three metric γ_{ij} .

2.2. Conservation of Energy and Lepton Number

As explained in Section 2.1, the formalism of our code that treats the radiation-hydrodynamics equations in a conservative form is suitable to satisfy the energy conservation of the total system (neutrinos and matters; see also Kuroda & Umeda 2010 and Kuroda et al. 2012 for more details). Let us first show how the energy conservation law is obtained in our code.

To focus only on the energy exchange between the matter and neutrino radiation field, we omit the gravitational source term in the following discussion. Then, the equations of energy conservation of matter and neutrinos (e.g., Equations (4) and

(11)) become

$$\partial_t \sqrt{\gamma} \tau + \partial_i \sqrt{\gamma} (\tau v^i + P(v^i + \beta^i)) = \int d\varepsilon \sqrt{\gamma} \alpha S_{(\varepsilon)}^\mu n_\mu, \quad (13)$$

$$\begin{aligned} & \partial_t \sqrt{\gamma} E_{(\varepsilon)} + \partial_i \sqrt{\gamma} (\alpha F_{(\varepsilon)}^i - \beta^i E_{(\varepsilon)}) + \sqrt{\gamma} \alpha \partial_\varepsilon (\varepsilon \tilde{M}_{(\varepsilon)}^\mu n_\mu) \\ &= -\sqrt{\gamma} \alpha S_{(\varepsilon)}^\mu n_\mu. \end{aligned} \quad (14)$$

From the above two equations, one can readily see that the total energy (sum of matter and neutrinos) contained in the computational domain, $E_{\nu m} \equiv \int dx^3 \sqrt{\gamma} (\tau + \int d\varepsilon E_{(\varepsilon)})$, is conserved in our basic equations as long as there is no net energy flux through the numerical and momentum space boundaries (i.e., $\int d\varepsilon [\partial_\varepsilon (\varepsilon \tilde{M}_{(\varepsilon)}^\mu n_\mu)] = 0$).

The lepton number conservation needs to be satisfied with good accuracy because it determines the PNS mass and the postbounce supernova dynamics. We here explain how we treat it in our code. As for the electron and neutrino number conservation, the basic equations are given by

$$\begin{aligned} & \partial_t \left(\frac{\rho_* Y_e}{m_u} \right) + \partial_i \left(\frac{\rho_* Y_e v^i}{m_u} \right) \\ &= \sqrt{\gamma} \alpha \int \frac{d\varepsilon}{\varepsilon} (S_{(\nu_e, \varepsilon)}^\mu - S_{(\bar{\nu}_e, \varepsilon)}^\mu) u_\mu, \end{aligned} \quad (15)$$

$$\begin{aligned} & \partial_t (q_{(\varepsilon)}^0 \sqrt{\gamma} \alpha) + \partial_i (q_{(\varepsilon)}^i \sqrt{\gamma} \alpha) - \sqrt{\gamma} \alpha \partial_\varepsilon (\varepsilon q_{(\varepsilon)}^{\alpha\beta}) \nabla_\beta u_\alpha \\ &= -\frac{\sqrt{\gamma} \alpha}{\varepsilon} S_{(\varepsilon)}^\mu u_\mu, \end{aligned} \quad (16)$$

where

$$q_{(\varepsilon)}^\alpha \equiv -\varepsilon^{-1} T_{(\varepsilon)}^{\alpha\beta} u_\beta = (\mathcal{J}_{(\varepsilon)} u^\alpha + \mathcal{H}_{(\varepsilon)}^\alpha), \quad (17)$$

$$q_{(\varepsilon)}^{\alpha\beta} \equiv \varepsilon^{-1} T_{(\varepsilon)}^{\gamma\beta} h_\gamma^\alpha = (\mathcal{H}_{(\varepsilon)}^\alpha u^\beta + \mathcal{L}_{(\varepsilon)}^{\alpha\beta}), \quad (18)$$

with $(\mathcal{J}, \mathcal{H}^\alpha, \mathcal{L}^{\alpha\beta}) \equiv \varepsilon^{-1} (J, H^\alpha, L^{\alpha\beta})$. The conservation equation for neutrinos (16) corresponds to Equation (3.22) (divided by ε) in Shibata et al. (2011). Since the neutrino number density measured by an Eulerian observer is expressed as

$$n_{\nu, \text{Euler}} = \int d\varepsilon q_{(\nu_e, \varepsilon)}^0 \sqrt{\gamma} \alpha, \quad (19)$$

the equation of the total lepton number conservation becomes

$$\partial_t (\rho_* Y_l) + \partial_i \left(\rho_* Y_e v^i + m_u \sqrt{\gamma} \alpha \int d\varepsilon [q_{(\nu_e, \varepsilon)}^i - q_{(\bar{\nu}_e, \varepsilon)}^i] \right) = 0. \quad (20)$$

Here the total lepton fraction Y_l is defined by

$$\begin{aligned} Y_l &= Y_e + Y_{\nu_e} - Y_{\bar{\nu}_e} \\ &= Y_e + \frac{m_u}{\rho u^t} \int d\varepsilon (q_{(\nu_e, \varepsilon)}^0 - q_{(\bar{\nu}_e, \varepsilon)}^0). \end{aligned} \quad (21)$$

From Equation (20), one can readily see that the total lepton number is conserved irrespective of the included neutrino matter interaction processes in case there is no net flux through the numerical and energy space boundaries. The distribution of Y_l into the each component (e.g., $Y_e, Y_{\nu_e}, Y_{\bar{\nu}_e}$) is determined by the details of the implemented microphysics, which should be checked carefully and will be reported in Section 5.

2.2.1. Neutrino Number Transport in the Diffusion Limit

In the collapsing iron core, it is well known that the central core becomes opaque to neutrinos due mainly to scattering off heavy nuclei when the central density exceeds $\sim 10^{11-12} \text{ g cm}^{-3}$ (Sato 1975) and neutrinos are *trapped* with matter afterward. In the diffusion limit at large neutrino opacities, the trapped neutrinos move with the matter velocity v_i for an Eulerian observer. Thus, their advection equation can be described with the same form of Y_e as

$$\partial_t \rho_* Y_\nu + \partial_i \rho_* Y_\nu v^i = (\text{Source terms}). \quad (22)$$

Because the source terms in the above equation amount to equal the negative value of the source terms in the electron number conservation equation, the core lepton number is conserved with good accuracy until it gradually decreases by diffusion in the PNS cooling phase. Since the central core mass depends on the core lepton number, the CCSN simulation should be able to capture this important phenomena appropriately.

In our formalism, however, this is not a trivial problem because we solve the energy–momentum conservation in Equations (4)–(5) and not the neutrino number conservation in Equation (16). In this section, we check whether our basic equations can reproduce the neutrino diffusion limit adequately, i.e., they reach asymptotically to Equation (22).

For simplicity, we assume in the following that the spacetime is flat and the typical velocity of the matter field (v) is much smaller than the speed of light (slow motion limit; neglecting terms higher than the second order with respect to (v/c)).

Let us first check whether Equation (16) can satisfy the local neutrino number conservation in the trapped region. In this limit, the neutrino number density at each energy bin q^0 and its flux q^i approach

$$q^0 = \mathcal{J}u^t + \mathcal{H}^0 \sim \mathcal{J} + \frac{\mathcal{H}_i v^i}{W} \sim \mathcal{J}, \quad (23)$$

$$q^i = \mathcal{J}u^i + \mathcal{H}^i \sim \mathcal{J}v^i + \mathcal{H}^i \sim q^0(v^i + \mathcal{H}^i/\mathcal{J}). \quad (24)$$

From these relations, it is obvious that the neutrino number density at each energy bin q^0 is transferred with the matter velocity v^i plus the diffusion velocity $\mathcal{H}^i/\mathcal{J}$ and the equation of the total lepton number (Equation (20)) in the slow motion limit becomes

$$\begin{aligned} \partial_t(\rho_* Y_l) + \partial_i(\rho_* Y_e v^i + m_u \sqrt{\gamma} \alpha \int d\varepsilon [q_{(v_e, \varepsilon)}^0 - q_{(\bar{\nu}_e, \varepsilon)}^0] v^i) \\ = \partial_t(\rho_* Y_l) + \partial_i(\rho_* Y_l v^i) = 0, \end{aligned} \quad (25)$$

demonstrating that Equation (20) satisfies the local lepton number conservation in the trapped region.

Next, we take the diffusion limit of Equation (4). In this limit, H^i/J should approach 0 (i.e., the radiation flux (H^i) in the comoving frame vanishes). From this, the following relation can be derived:

$$H^i \sim -E v^i + F^i - P^{ij} v_j \sim 0 \implies F^i \sim \frac{4}{3} E v^i, \quad (26)$$

where we take a simple closure relation $P^{ij} = \frac{E}{3} \delta^{ij}$ in the diffusion limit. Inserting this into the left-hand side of

Equation (4), one can get

$$\begin{aligned} \partial_t E + \partial_i F^i + \partial_\varepsilon(-\varepsilon P^{ij} \partial_i v_j) \\ \sim \partial_t E + \partial_i \left(\frac{4}{3} E v^i \right) - \frac{E}{3} \delta^{ij} \partial_i v_j - \varepsilon (\partial_\varepsilon P^{ij}) \partial_i v_j \end{aligned} \quad (27)$$

$$\sim \partial_t E + \partial_i \left(\frac{4}{3} E v^i \right) - \partial_i \left(\frac{1}{3} E v^i \right) - \varepsilon (\partial_\varepsilon P^{ij}) \partial_i v_j \quad (28)$$

$$\sim \partial_t E + \partial_i (E v^i) - \varepsilon (\partial_\varepsilon P^{ij}) \partial_i v_j. \quad (29)$$

Moving from the rhs of Equation (27) to that of Equation (28), we assumed that E has almost no spatial gradient well below the neutrino spheres (at high opacities) in the prebounce core. This is satisfied quite well as shown in the literature (Bruenn 1985), in which a nearly flat Y_{ν_e} profile is shown in their standard models within the central core with mass $\sim 0.5\text{--}0.6 M_\odot$ after the central density exceeds $\sim 5 \times 10^{13} \text{ g cm}^{-3}$. Note that in Equation (28) the third term $-\partial_i(E v^i/3)$, which is originally a part of the advection terms in the energy space $\partial_\varepsilon(-\varepsilon P^{ij} \partial_i v_j)$, balances with part of the spatial advection term $\partial_i(4E v^i/3)$ and they lead to the second term in Equation (29). From this, one can clearly see how the *apparent* advection speed of E at each energy bin ε approaches the matter velocity v^i in the diffusion limit. Then, assuming that the neutrino number density at each energy bin can be approximately expressed as

$$q^0 \sim \mathcal{J} \sim \mathcal{E} - 2\mathcal{F}^i v_i \sim \mathcal{E}, \quad (30)$$

in the slow motion limit, when we divide Equation (29) by ε and integrate it in energy space, it can be summarized as

$$\int d\varepsilon [\partial_t q^0 + \partial_i(q^0 v^i) - (\partial_\varepsilon P^{ij}) \partial_i v_j] = \partial_t n_\nu + \partial_i n_\nu v^i. \quad (31)$$

From this, one can clearly see that the neutrino number density $n_\nu (= \rho Y_\nu)$ is transported with the same matter velocity v^i in the diffusion limit.

3. NUMERICAL METHOD

In this section, we describe how to evolve the radiation-hydrodynamics variables.⁸ As we explained in the previous section, we solve Equations (4), (5), and (9)–(12) as our basic equations which are collectively expressed as

$$\partial_t \mathcal{Q} + \mathcal{S}_{\text{adv},s} + \mathcal{S}_{\text{adv},e} + \mathcal{S}_{\text{grv}} + \mathcal{S}_{\nu m} = 0, \quad (32)$$

where \mathcal{Q} denotes conservative variables

$$\mathcal{Q} = \begin{bmatrix} \rho_* \\ \sqrt{\gamma} S_i \\ \sqrt{\gamma} \tau \\ \rho_* Y_e \\ \sqrt{\gamma} E_{(v, \varepsilon)} \\ \sqrt{\gamma} F_{(v, \varepsilon)_i} \end{bmatrix}. \quad (33)$$

In Equation (32), $\mathcal{S}_{\text{adv},s}$, $\mathcal{S}_{\text{adv},e}$, \mathcal{S}_{grv} , and $\mathcal{S}_{\nu m}$ denote the advection term in space, the advection term in momentum space, the gravitational source, and the neutrino–matter interaction term, respectively. Throughout this paper, with the exception of Appendix B, we divide this equation into the following

⁸ We omit our numerical method to evolve the spacetime variables that are essentially the same as in Kuroda et al. (2012).

two parts, which are expressed in the finite difference expression as

$$\frac{\mathbf{Q}^* - \mathbf{Q}^n}{\Delta t} + \mathbf{S}_{\text{adv},s}^n + \mathbf{S}_{\text{grv}}^n = 0, \quad (34)$$

for the explicit part and

$$\frac{\mathbf{Q}^{n+1} - \mathbf{Q}^*}{\Delta t} + \mathbf{S}_{\text{adv},e}^{n+1} + \mathbf{S}_{\nu\text{m}}^{n+1} = 0, \quad (35)$$

for the implicit part, respectively. In Equations (34)–(35), Δt is the time step size between the n th and $n + 1$ th time steps and the upper indices “ n ” represents the n th time step. Variables with “*” denote the time updated variables during an operator-splitting procedure.

In Equation (34), $\mathbf{S}_{\text{adv},s}^n$ and $\mathbf{S}_{\text{grv}}^n$ represent the terms with respect to advection in space and gravitational fields at the n th time step, both of which are added first in an explicit manner to obtain conservative variables at a middle time step \mathbf{Q}^* . Next, in Equation (35), the rest of terms, advection in energy space ($\mathbf{S}_{\text{adv},e}$) and neutrino–matter interaction terms ($\mathbf{S}_{\nu\text{m}}$) at $(n + 1)$ th time step, are added to \mathbf{Q}^* in order to find the converged solution of \mathbf{Q}^{n+1} by an iterative method. We separate the source terms into the two parts, explicit and implicit ones, because the typical time step size, $\Delta t \sim 4 \times 10^{-7}$ s, which is determined by the speed of light c , typical minimum grid width in our calculation $\Delta x \sim 500$ m, and the Courant–Friedrichs–Lewy number CFL, e.g., 0.25, is sufficiently short for the advection term in space $\mathbf{S}_{\text{adv},s}$ and the gravitational source term \mathbf{S}_{grv} as well as for all the geometrical variables by an explicit update. However, it is too long to follow, e.g., the weak interaction term, which has a significantly shorter timescale ($\lesssim 10^{-9}$ s). We thus need to treat these terms in an implicit way through Equation (35) to ensure a numerical convergence and stability.

Here, we should comment on the treatment of the advection terms in energy space $\mathbf{S}_{\text{adv},e}$. As we mentioned above, we solve them implicitly in time as Equation (35) in our main results. It means that there is a time gap Δt between the moment of the evaluation for advection terms in real space $\mathbf{S}_{\text{adv},s}^n$ and that in energy space $\mathbf{S}_{\text{adv},e}^{n+1}$. Although we can generally obtain consistent results with previous studies regardless of the time gap, it is noted that the treatment of the energy advection either by the implicit or explicit scheme leads to visible changes in the postbounce features. We will discuss this point further in Appendix B.

In the following sections, we describe how to evaluate the advection terms in space (Section 3.1) and in energy space (Section 3.2), and then move on to describe the implicit time update in Section 3.3.

3.1. Advection in Space

We employed a standard high-resolution, shock-capturing scheme and utilize the HLL (Harten–Lax–van Leer) scheme (Harten et al. 1983) to evaluate the numerical fluxes in space (Kuroda & Umeda 2010). As for the fastest and slowest characteristic wave speeds of the radiation field system (Equations (4) and (5)), we again use the same definition as in Kuroda et al. (2012; see also Shibata et al. 2011) and connect $\lambda_{\text{rad,thin}}$ and $\lambda_{\text{rad,thick}}$ smoothly via the variable

Eddington factor χ as

$$\lambda_{\text{rad}} = \frac{3\chi - 1}{2} \lambda_{\text{rad,thin}} + \frac{3(1 - \chi)}{2} \lambda_{\text{rad,thick}}, \quad (36)$$

where $\lambda_{\text{rad,thin}}$ and $\lambda_{\text{rad,thick}}$ are the wave speed in the optically thin and thick limits, respectively.

To enforce the numerical flux of the radiation field in the opaque region as it asymptotically approaches the diffusion limit, we evaluate the energy flux (F_{hill}^0) and the momentum flux (F_{hill}^i) as

$$F_{\text{hill}}^0 = \frac{\tilde{\lambda}_+ F_L^0 - \tilde{\lambda}_- F_R^0 + \epsilon \tilde{\lambda}_- \tilde{\lambda}_+ (Q_R^0 - Q_L^0)}{\tilde{\lambda}_+ - \tilde{\lambda}_-}, \quad (37)$$

and

$$F_{\text{hill}}^i = \frac{\epsilon^2 (\tilde{\lambda}_+ F_L^i - \tilde{\lambda}_- F_R^i) + \epsilon \tilde{\lambda}_- \tilde{\lambda}_+ (Q_R^i - Q_L^i)}{\tilde{\lambda}_+ - \tilde{\lambda}_-} + (1 - \epsilon^2) \frac{F_L^i + F_R^i}{2}, \quad (38)$$

respectively (Audit et al. 2002; O’Connor & Ott 2013). Here, $Q_{L/R}^\alpha$ and $F_{L/R}^\alpha$ are the conservative variables and their corresponding fluxes, respectively, with L/R denoting the left/right states for the Riemann problem. All the radiation-hydrodynamical variables are defined at the cell center. For those cell centered (primitive) variables, we use a monotonized central reconstruction, which has second order accuracy in space, and obtain left/right states at the cell surface (see Kuroda & Umeda 2010 for a more detailed explanation). After the reconstruction, all the characteristic wave speeds of the matter and radiation fields are evaluated.

ϵ is a modification parameter to fit the numerical flux to the diffusion limit, which we take as

$$\epsilon = \min\left(1, \frac{1}{\kappa \Delta x}\right), \quad (39)$$

where κ is the total opacity and Δx is the grid width (Audit et al. 2002; O’Connor & Ott 2013).

3.2. Advection in Energy Space

Regarding the advection term in energy space in all conservation equations (Equations (4), (5), and (16)), we define the advection fluxes at the interface of the energy bin as the same as in Müller et al. (2010) so that all energy-integrated advection terms will vanish. This can be achieved since both terms, \tilde{M}^α , appearing in energy and momentum conservation equations, and $\epsilon q^{\alpha\beta}$ in number conservation equation, are expressed in terms of linear combinations of radiation momenta, J , H^α , $L^{\alpha\beta}$..., and we therefore can define their cell surfaced values with an appropriate weighting function to suppress the violation of all conservations simultaneously.

For all orders of the radiation momenta $X \in \{J, H^\alpha, L^{\alpha\beta} \dots\}$, the following conditions need to be satisfied for number conservation,

$$\int d\epsilon \partial_\epsilon X = 0 \implies \sum_i \Delta \epsilon_i \frac{X_{i+1/2} - X_{i-1/2}}{\Delta \epsilon_i} = 0, \quad (40)$$

and for energy and momentum conservations,

$$\int d\varepsilon \partial_\varepsilon (\varepsilon X) = \int d\varepsilon (\varepsilon \partial_\varepsilon X + X) = 0$$

$$\Rightarrow \sum_i \Delta \varepsilon_i \left[\varepsilon_i \frac{X_{i+1/2} - X_{i-1/2}}{\Delta \varepsilon_i} + X_i \right] = 0, \quad (41)$$

respectively. The rhs of the above equations represent the finite difference expressions with i and $i + 1/2$ denoting the i th energy bin and the interface between the i - and $(i + 1)$ th energy bins, respectively. $\Delta \varepsilon_i$ is the energy grid width $\Delta \varepsilon_i = \varepsilon_{i+1/2} - \varepsilon_{i-1/2}$. It is straightforward to show that Equation (40) can be automatically satisfied for any cell surfaced quantities as long as they vanish at the outer boundary in the energy space. By introducing a definition $X_{i+1/2} \equiv X_i^L + X_{i+1}^R$, the rhs of Equation (41) can be expressed as

$$\sum_i [-(\varepsilon_{i+1} - \varepsilon_i) X_i^L - (\varepsilon_i - \varepsilon_{i-1}) X_i^R + \Delta \varepsilon_i X_i] = 0. \quad (42)$$

As in Müller et al. (2010), we can get the solution of Equation (42) as

$$X_i^L \equiv \frac{\Delta \varepsilon_i}{\varepsilon_{i+1} - \varepsilon_i} X_i \xi_i, \quad (43)$$

$$X_i^R \equiv \frac{\Delta \varepsilon_i}{\varepsilon_i - \varepsilon_{i-1}} X_i (1 - \xi_i), \quad (44)$$

where ξ_i is a weighting function and is expressed as

$$\xi_i \equiv \frac{f_{i+1/2}^\sigma}{f_{i-1/2}^\sigma + f_{i+1/2}^\sigma}. \quad (45)$$

In this study, we used a ‘‘Harmonic’’ interpolation ($\sigma = 1$) for the energy density ($f_{i+1/2}^\sigma$) as

$$f_{i+1/2}^\sigma \equiv \left[\left(\frac{E(\varepsilon_i)}{\varepsilon_i^3} \right)^{1-r_{i+1/2}} \left(\frac{E(\varepsilon_{i+1})}{\varepsilon_{i+1}^3} \right)^{r_{i+1/2}} \right]^\sigma, \quad (46)$$

with $r_{i+1/2} = (\varepsilon_{i+1/2} - \varepsilon_i) / (\varepsilon_{i+1} - \varepsilon_i)$ (see Müller et al. 2010 for more details). Like these, just only by evaluating an appropriate radiation momenta $X_{i+1/2}$ at the energy bin surface, we can simultaneously vanish Equations (40)–(41) numerically and maintain energy, momentum, and number conservations.

3.3. Implicit Time Update

After the explicit update, we solve the following simultaneous equation (e.g., Equation (35));

$$f(\mathbf{P}^{n+1}) \equiv \frac{\mathbf{Q}(\mathbf{P}^{n+1}) - \mathbf{Q}^*}{\Delta t} + \mathbf{S}_{\text{adv,e}}(\mathbf{P}^{n+1}) + \mathbf{S}_{\nu\text{m}}(\mathbf{P}^{n+1}) = 0, \quad (47)$$

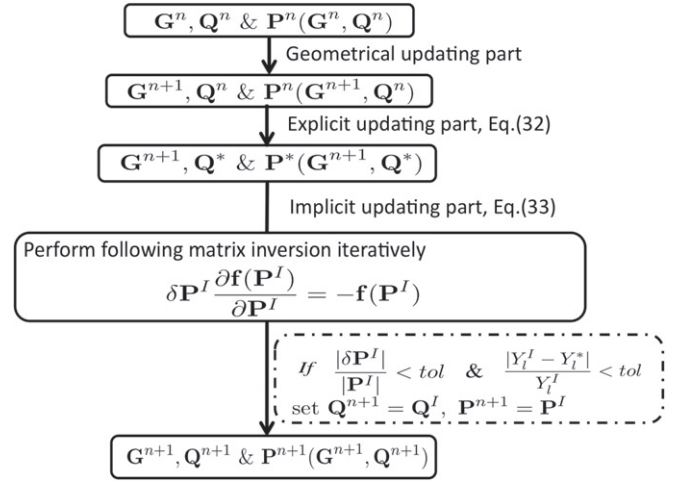


Figure 1. Flow chart to visualize how to update variables (G , Q , and P) from the n th to the $(n + 1)$ th time step (see the text).

where Q , $S_{\text{adv,e}}$, and $S_{\nu\text{m}}$ are expressed in terms of the primitive variables P

$$\mathbf{P} = \begin{bmatrix} \rho \\ u_i \\ s \\ Y_e \\ E_{(\nu,\varepsilon)} \\ F_{(\nu,\varepsilon)_i} \end{bmatrix}, \quad (48)$$

at the $(n + 1)$ th time step. Obviously, the baryon number density does not change in this step, i.e., $\rho^* = \rho^{n+1}$. To get the solutions of the above simultaneous equation, we employ the Newton–Raphson iteration scheme with the inversion of the following matrix until a sufficient convergence is achieved:

$$\frac{\partial f(\mathbf{P}^I)}{\partial \mathbf{P}} \delta \mathbf{P}^I = -f(\mathbf{P}^I), \quad (49)$$

$$\mathbf{P}^{I+1} = \mathbf{P}^I + \delta \mathbf{P}^I, \quad (50)$$

for $I = 0, 1, 2, \dots$, with the initial condition $\mathbf{P}^0 = \mathbf{P}^*$. As for the convergence criteria for the Newton–Raphson iteration, we monitor

$$\frac{|\delta \mathbf{P}^I|}{|\mathbf{P}^I|} < \text{tol}, \quad (51)$$

where tol represents a tolerance and we typically set $\text{tol} = 10^{-8}$.

We note that even if we evaluate the advection terms in energy space explicitly in time as $S_{\text{adv,e}}^n$, Equations (47)–(51) do not change except the term $S_{\text{adv,e}}(\mathbf{P}^{n+1})$ in Equation (47) is now moved to the explicit part.

Our method for time update from the n th to $(n + 1)$ th time step is summarized as follows and schematically drawn in Figure 1.

1. Geometrical Update. We first evolve all the BSSN and the gauge variables $\mathbf{G} = \{\tilde{\gamma}_{ij}, \tilde{A}_{ij}, \phi, K, \tilde{\Gamma}^i, \alpha, \beta^i\}$ from the n th to the $(n + 1)$ th time step.
2. Explicit Update. In the second step, all the advection in space ($S_{\text{adv,s}}$) and gravitational source (S_{grv}) terms are added to obtain the fractional time step values

\mathbf{Q}^* and their consistent primitive variables $\mathbf{P}(\mathbf{G}^{n+1}, \mathbf{Q}^*) = (\rho, u_i, s, Y_e, E_{(\nu, \epsilon)}, F_{(\nu, \epsilon)_i})$. Advection of the total lepton number (Equation (20)) is also performed simultaneously to evaluate Y_l^* .

3. **Implicit Update.** Finally, quantities in the fractional time step (\mathbf{Q}^*) are implicitly updated to those in the $(n+1)$ th time step (\mathbf{Q}^{n+1}) by the Newton–Raphson iteration until a sufficient convergence is obtained with a constraint that the local lepton fraction does not change (i.e., $Y_l^{n+1} = Y_l^*$ since $\rho^{n+1} = \rho^*$) in the diffusion region.

Here we shortly summarize some technical details to achieve a sufficient lepton number conservation in practical core-collapse simulations. As we have already mentioned in Section 2.2, neutrino number conservation is formally satisfied by solving the energy–momentum conservation Equations (4)–(5). Especially, in the neutrino trapping regime, solving the energy conservation (Equation (4)) is practically identical to solving the neutrino number conservation (Equation (16)) which was proven in Section 2.2.1. However, in the finite difference method, it does not guarantee a perfect match between Equations (4)–(5) and (16) due to a discretization error. To minimize the difference, we add the following constraint to Equation (51)

$$\frac{|Y_l^I - Y_l^*|}{Y_l^I} < \text{tol}, \quad (52)$$

as another criterion to exit the Newton–Raphson iteration. Because of this additional criterion, the lepton number conservation is also satisfied when the Newton–Raphson iteration converges. Note that the local baryon numbers do not change in Equation (47), i.e., $Y_l^* = Y_l^{n+1}$ should be met if the lepton number is conserved.

We also adopt another prescription in which Y_l^{n+1} is used to achieve a better convergence for the Newton–Raphson method. In some cases, Y_e^I happens to go beyond the range of the employed EOS table during the iteration, especially when the Jacobian matrix is not well evaluated. In those cases, we use Y_l^{n+1} to reset Y_e^I as below:

$$Y_e^I = Y_l^{n+1} - Y_{\nu_e}^I + Y_{\bar{\nu}_e}^I. \quad (53)$$

With this reset, we found that Y_e^I hardly goes beyond the range of the EOS table and also does not take an unreasonable value for the supernova core. In addition, the number of the Newton–Raphson iteration can sometimes be reduced. This is because the reset value Y_e^I automatically satisfies the lepton number conservation $Y_l^I = Y_e^I + Y_{\nu_e}^I - Y_{\bar{\nu}_e}^I = Y_l^{n+1}$, which leads to faster convergence.

Without these two prescriptions, we observed that the central lepton fraction at bounce deviates maximally ~ 0.05 from the value immediately after neutrino trapping sets in ($\rho_c \gtrsim 10^{12} \text{ g cm}^{-3}$). Note that these ad hoc constraints are introduced just to find a more efficient path toward convergence in the implicit time update. The criterion for convergence is solely given by Equation (51). Since we do not include Equation (20) into (47), there is no inconsistency between the number of simultaneous equations $f(\mathbf{P})$ and the unknown variables \mathbf{P}^{n+1} .

4. RADIATION TESTS

In this section, we show the results of several simple test problems to check the validity of our M1 radiation transport code. Except for Section 4.4, a flat spacetime is assumed throughout this section.

4.1. Diffusion Wave Test

We first perform a diffusion wave test, by which we check the validity of our flux implementation in the diffusion limit. Following Pons et al. (2000), a Dirac δ -function-type radiation source is initially located at $r=0$. Then we follow the diffusion of the source into the optically thick medium with zero absorptivity ($\kappa_a = 0$) and high scattering opacity ($\kappa_s = 10^2, 10^5$). The source term in Equations (4)–(5) thus becomes

$$S^\mu = -\kappa_s H^\mu. \quad (54)$$

The 3D computational domain is covered by 100 equidistant Cartesian zones in each direction ($x \in [-0.5, 0.5]$) for a model with $\kappa_s = 10^2$. This corresponds to a Peclet number $Pe = \kappa_s \Delta x = 1$. While in the other model with $\kappa_s = 10^5$ we raise the nested level to 2 to achieve sufficient resolution at the center and to check that the nested structure does not interfere with the radiation propagation in the diffusion limit. In this model, 32^3 numerical cells cover the base domain $x \in [-0.5, 0.5]$ with a nested level of 2. The minimum grid width and Peclet number at the center are thus $\Delta x = 1/128 \sim 0.78$ and $Pe = 10^5/128 \sim 780$, respectively. Since Pe is much higher than unity, ϵ in Equation (39) approaches zero, which enables us to check whether the radiation transport in the diffusion limit is solved appropriately.

The analytical solution of the zeroth and first order radiation momenta profiles at time T (Pons et al. 2000) is given as

$$E(r, T) = \left(\frac{\kappa_s}{T}\right)^{3/2} \exp\left(\frac{-3\kappa_s r^2}{4T}\right), \quad (55)$$

$$F_r(r, T) = \frac{r}{2T} E, \quad (56)$$

respectively. From Figure 2, it can be seen that our code can reproduce the analytical results quite well.

4.2. Shadow Casting Test

Next, we move on to a shadow casting test to check the ability of our code and whether the anisotropic radiation field can be appropriately evolved in the free streaming limit. The initial setup is essentially the same as in Kanno et al. (2013). We set a perfect absorbing region at $x \in [2, 3]$ and $\{y, z\} \in [-2, 2]$ inside the numerical domain $x \in [0, 12]$ and $\{y, z\} \in [-4, 4]$. We impose a constant radiation $(E, F_x) = (1, f_{\max})$ from the left boundary. Numerical resolution is $\Delta x (= \Delta y = \Delta z) = 12/192$ and we set $f_{\max} = 0.999$. Within the perfect absorbing region, the absorbing opacity is set as $\kappa_a \Delta x \sim 10^{10}$, otherwise $\kappa_a = 0$. The source term in Equations (4)–(5) thus becomes

$$S^\mu = -\kappa_a ((J - J^{\text{eq}})u^\mu + H^\mu), \quad (57)$$

with $J^{\text{eq}} = 0$ and $u^\mu = (1, 0, 0, 0)$. In Figure 3, we show three different time snapshots ($T = 3.5, 7.5,$ and 15.5) of the radiation energy density in a logarithmic scale. The absorbing

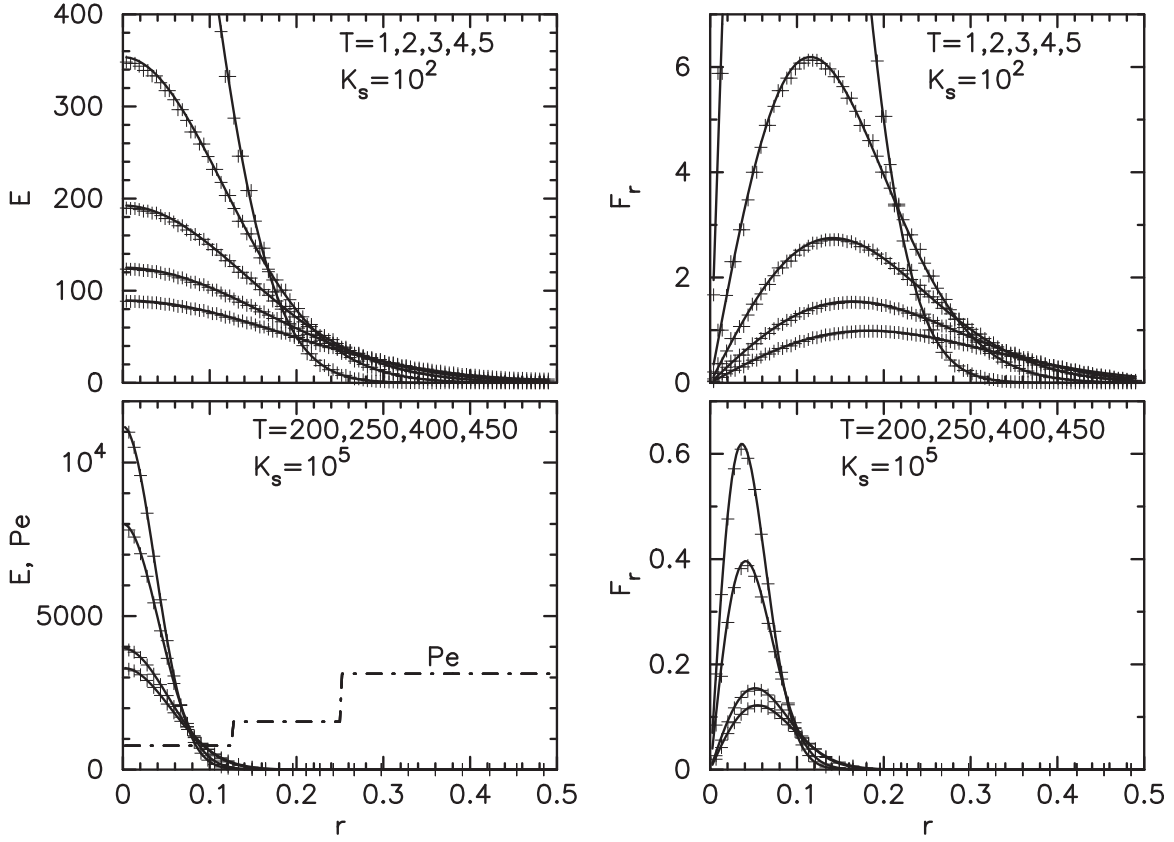


Figure 2. Diffusion tests with $\kappa_s = 10^2$ ($Pe = \kappa_s \Delta x = 1$) in the upper two panels and with $\kappa_s = 10^5$ ($Pe \gtrsim 780$) in the bottom two. Our results (crosses) for the evolutions of the energy density (left panels) and radial energy flux (right panels) are compared with the analytical ones (solid lines). Note that the simulations start at $T = 1$ and 200 for models with $\kappa_s = 10^2$ and $\kappa_s = 10^5$, respectively. The model with $\kappa_s = 10^5$ is performed with two nested level structure and we plot the spatial profile of Pe in the bottom left panel for reference. Note that we reduce number of plots for our results (crosses) to avoid overplotting.

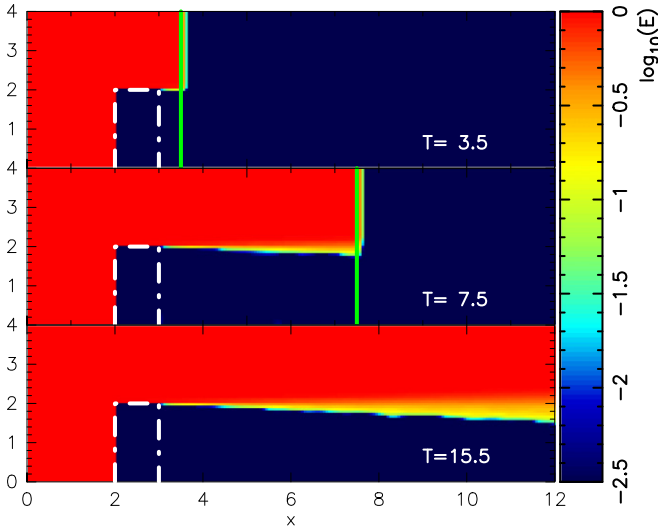


Figure 3. Shadow test at different time slices $T = 3.5, 7.5,$ and 15.5 from top to bottom. Color contours represent the radiation energy density on a logarithmic scale. The absorbing region is expressed by the white dashed line and the expected radiation shock front (i.e., $x = T$) is denoted by a vertical green line.

region is expressed by white dashed line and the radiation shock front ($x = T$) is denoted by a vertical green line. From this figure, we see that the absorbing condition works appropriately in our scheme and the radiation front propagates

with the light speed $v = 1$. Furthermore, the region beyond the absorbing box is barely contaminated by the radiation. These features are in good agreement with Kanno et al. (2013).

4.3. Propagation in Free Streaming Regime

The next test is a spherical expansion of the radiation field from a point-like source into an optically thin medium. The aim of this test is to check whether our code using the Cartesian coordinates can maintain the sphericity of the field during the expansion. By following Just et al. (2015), we define the radiation source \mathcal{S} with radius $r_S = 1.5$ which centers at the origin of the 2D Cartesian domain with $\mathbf{x} \in [-7.5, 7.5]$. We also define the purely absorbing region \mathcal{A} centered at $\mathbf{x} = (3.5, 0)$ with radius $r_A = 1$. Inside those two regions, the absorptivity $\kappa_a(\mathbf{x})$ and equilibrium energy density $J^{\text{eq}}(\mathbf{x})$ are set as

$$\kappa_a(\mathbf{x}) = \begin{cases} 10 \exp\{-(4\sqrt{x^2 + y^2}/r_S)^2\}, & \mathbf{x} \in \mathcal{S} \\ 10, & \mathbf{x} \in \mathcal{A}, \end{cases} \quad (58)$$

and

$$J^{\text{eq}}(\mathbf{x}) = \begin{cases} 10^{-1}, & \mathbf{x} \in \mathcal{S} \\ 0, & \mathbf{x} \in \mathcal{A}, \end{cases} \quad (59)$$

respectively. In other regions, we set $\kappa_a(\mathbf{x}) = 0$ and $J^{\text{eq}}(\mathbf{x}) = 0$. We neglect the scattering opacity $\kappa_s(\mathbf{x})$. The source term in Equations (4)–(5) is thus the same as

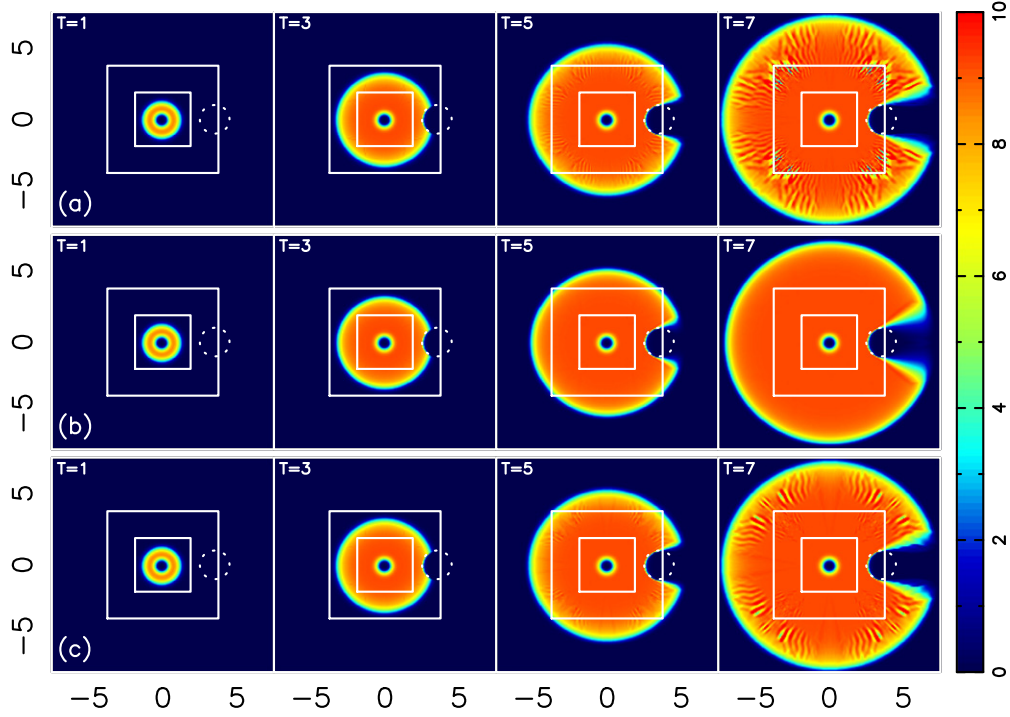


Figure 4. Time snapshots of the spherical explosion test in the optically thin medium with different sets of $(f_{\max}, \lambda_{\pm})$. Models (a) and (c) (top and bottom rows) are models taking $f_{\max} = 1$, while $f_{\max} = 0.93$ is taken in model (b) (middle row). Equations (64) and (65) are used in models (a)-(b) and (c), respectively. Color scale represents radiation energy density on a linear scale in arbitrary units. The inner two squares represent the boundary of the nested structure and the dotted circle shows the purely absorbing region \mathcal{A} .

Equation (57). Regarding the initial setup for the zeroth and first order momenta of radiation field, we assume an arbitrary dilute radiation field as

$$E = 10^{-9} \quad (60)$$

$$|F|/E = 10^{-10}. \quad (61)$$

The 2D numerical domain is covered by 196 equally distant Cartesian zones in each direction with two nested levels, i.e., Δx varies from 15/784 to 15/196.

In this test, we use the following formula for the variable Eddington factor χ (Levermore 1984):

$$\chi = \frac{3 + 4\bar{F}^2}{5 + 2\sqrt{4 - 3\bar{F}^2}}. \quad (62)$$

Only in this propagation test, we take two possible options for evaluating the characteristic wave speeds of the radiation field in the optically thin limit λ_{\pm} . Assuming a flat spacetime and using the following closure relation in the optically thin limit

$$P^{\mu\nu} = E \frac{F^{\mu} F^{\nu}}{F_k F^k}, \quad (63)$$

the first one is (Shibata et al. 2011)

$$\lambda_{\pm}^{S,i} = \max/\min \left[\frac{EF^i}{F_k F^k}, \pm \frac{F^i}{\sqrt{F_k F^k}} \right], \quad (64)$$

and the second one is (Skinner & Ostriker 2013)

$$\lambda_{\pm}^{SO,i} = \left\{ \mu^i \bar{F} \pm \sqrt{\frac{2}{3} (4 - 3\bar{F}^2 - \sqrt{4 - 3\bar{F}^2}) + 2\mu^{i2} (2 - \bar{F}^2 - \sqrt{4 - 3\bar{F}^2})} \right\} / \sqrt{4 - 3\bar{F}^2}. \quad (65)$$

Here, $\mu^i \equiv \cos \theta$ is determined by the angle θ which defines the orientation of the energy flux F relative to the interface normal x^i . Note that in the rest of the paper we use only Equation (64) for the free streaming part.

Also of note, we limit the flux factor $f \equiv \sqrt{\gamma^i F_i F_j} / E$ to be less than the maximum allowed value f_{\max} by modifying the first-order moment as

$$F_i \rightarrow \min(f_{\max}/f, 1) F_i, \quad (66)$$

in every time step. Note that setting $f_{\max} < 1$ means that we add contribution from the isotropic radiation pressure P_{thick}^{ij} according to Equation (6). The reason of this modification will be discussed later in this section.

In Figure 4, we show results for three different models taking different values for f_{\max} and using different evaluation formulae for $\lambda_{\pm}^{S/SO}$. The upper two panels (panels (a) and (b)) and the bottom one (panel (c)) are models using Equations (64) and (65), respectively. In panels (a) and (c), we take $f_{\max} = 1$, while $f_{\max} = 0.93$ is taken in panel (b). The color represents the energy density E in a logarithmic scale at four different time slices ($T = 1, 3, 5, 7$). The inner two squares represent the boundary of the nested structure and the dotted circle shows the purely absorbing region \mathcal{A} . From models (a) and (c), which use $f_{\max} = 1$, we find non-isotropy which can be seen as corrugated patterns behind the radiation front, obviously with the exception of the absorbing circle \mathcal{A} and its shadowing region. Furthermore, in model (a) at $T = 7$, another remarkable violation of isotropy is seen at 45° away

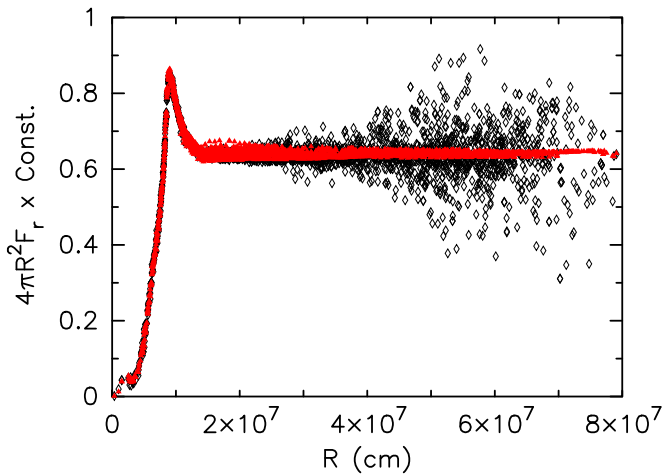


Figure 5. Arbitrary normalized surface-integrated local neutrino luminosities measured by an Eulerian observer. The background profile is a stationary and spherically symmetric SN core taken at the postbounce time 100 ms. Models are with two different maximum allowed flux factors, $f_{\max} = 0.999$ (black diamonds) and $= 0.93$ (red filled triangles).

from the coordinate axes. Note that from snapshot at $T = 7$ in panel (a), this violation seems to be associated with the nested structure. We, however, confirmed that this is not the artifact of that by performing a run with a zero nested level. By comparing models (a) and (c), the violation seen at 45° is eliminated in model (c). Model (c) takes into account the propagation angle (μ^i) relative to the interface normal more explicitly than model (a) when we evaluate $\lambda_{\pm}^{\text{SO}}$. We therefore consider a more accurate evaluation in the characteristic wave speeds λ_{\pm} for the numerical flux (Equations (37)–(38)) is key to follow the radiation in an optically thin limit properly. While in panel (b), in which we use $f_{\max} = 0.93$, we do not see any spherical symmetry breaking.

We also apply this test to a supernova core profile. We fix the hydrodynamical background, which has a typical core profile at $T_{\text{pb}} \sim 100$ ms, and follow only the propagation of neutrino radiation. The neutrino transport part is identical to our practical calculation reported later in Section 5 and all relevant neutrino–matter interactions, gravitational redshift, and Doppler shift terms are taken into account. There is thus a transition from an optically thick to a thin regime. We calculate two models with different values for f_{\max} . $\lambda_{\pm}^{\text{S},i}$ (Equation (64)) is used in both models to evaluate the characteristic wave speeds. In Figure 5, we show the radial profiles of (electron-type) neutrino luminosity for two cases: one is calculated with $f_{\max} = 0.999$ (black diamonds) and the other is with $f_{\max} = 0.93$ (red filled triangles). As can be clearly seen, beyond the shock position ($R \gtrsim 100$ km) where it is optically thin regime, a large scatter is seen at $R \gtrsim 300$ – 400 km for a model with $f_{\max} = 0.999$. The spatial location of the highly deviated radiation is again concentrated $\sim 45^\circ$ away from the coordinate axes, which is the same as in the previous simple propagation test (panel (a) in Figure 4). Meanwhile, in model with $f_{\max} = 0.93$, there is little deviation and the surface-integrated local luminosity stays nearly constant in the transparent region, as it should be.

From these two tests, we are currently enforced to set a ceiling value for the flux factor $f \leq f_{\max} = 0.93$ in the practical core-collapse simulation to follow spherical-like propagation stably. Since $f_{\max} = 1$ is the physically correct value, one may

suspect that our modification can be an obstacle for comparison of the emergent radiation profile with previous studies. From previous fully relativistic Boltzmann transport simulation (Liebendörfer et al. 2001), however, it was shown that the flux factor higher than, e.g., ~ 0.93 appears only beyond $R \gtrsim 500$ – 1000 km. Therefore, even if we evaluate the emergent neutrino profile at the same radius $R = 500$ km as previous studies, it is altered only slightly by a few percent and the modification cannot be a significant obstacle in this study. Obviously, the SN hydrodynamics itself is not affected by our artificial treatment since it is applied only to the optically thin region.

4.4. Gravitational Redshift and Doppler Shift

To check the energy-coupling terms for gravitational redshift and Doppler shift, $\sqrt{\gamma} \alpha \partial_{\epsilon} (\epsilon \tilde{M}_{(\epsilon)}^{\mu} n_{\mu})$ and $\sqrt{\gamma} \alpha \partial_{\epsilon} (\epsilon \tilde{M}_{(\epsilon)}^{\mu} \gamma_{i\mu})$ in Equations (4)–(5), we repeat the same tests performed in Müller et al. (2010) and O’Connor (2014). We consider the propagation of radiation from a sphere with radius $R = 10$ km through a curved spacetime and sharp velocity profile in spherical symmetry. Regarding the sharp velocity profile, we take the following:

$$u_r = \begin{cases} 0, & r \leq 70 \text{ km} \\ -0.2c \left(\frac{r - 70 \text{ km}}{10 \text{ km}} \right), & 70 \text{ km} \leq r \leq 80 \text{ km} \\ -0.2c \left(\frac{80 \text{ km}}{r} \right)^2, & r \geq 80 \text{ km}. \end{cases} \quad (67)$$

Here, u_r is the radial component of u_i . As for the curved spacetime, we take the same energy density profile for matter which is used in the second test problem in Section 4.3 and solve the Hamiltonian constraint to obtain the conformal factor ψ and lapse α . When we solve the Hamiltonian constraint, we assume a zero velocity profile ($v_i = 0 = \beta_i$) and the conformally flat approximation ($\gamma_{ij} = \psi^4 \tilde{\gamma}_{ij} = \psi^4 \delta_{ij}$). As for the initial neutrino profile within the radiating sphere, we take the zero chemical potential $\mu_{\nu} = 0$ and a temperature of 5 MeV, i.e., $\langle \epsilon \rangle \sim 15.7$ MeV, in the free streaming limit $E = \sqrt{\gamma_{ij} F^i F^j}$. Here $\langle \epsilon \rangle$ is the mean energy of neutrinos as measured in the comoving frame. Outside of the central radiating sphere, we choose an arbitrary dilute radiation field with $\langle \epsilon \rangle \sim 15.7$ MeV. We do not evolve neutrinos inside the radiating sphere and follow the propagation only at $R \geq 10$ km. The 3D computational domain is a cubic box with 3000 km width (i.e., the outer boundary is at the radius of 1500 km from the origin) and nested boxes with 7 refinement levels are embedded. Each box contains 64^3 cells and the minimum grid size near the origin is $\Delta x = 366$ m. As for the energy grid of the neutrino radiation field, we use logarithmically spaced 20 energy bins ($N_{\epsilon} = 20$) which center from $\epsilon = 1$ to 300 MeV. We calculate two models with and without the sharp velocity profile. Both models are calculated in the curved spacetime.

For the given velocity and spacetime profiles, the free streaming neutrinos propagate by obeying the following relations (Müller et al. 2010; O’Connor 2014):

$$W\alpha(1 + v_r)\langle \epsilon \rangle = \text{const}, \quad (68)$$

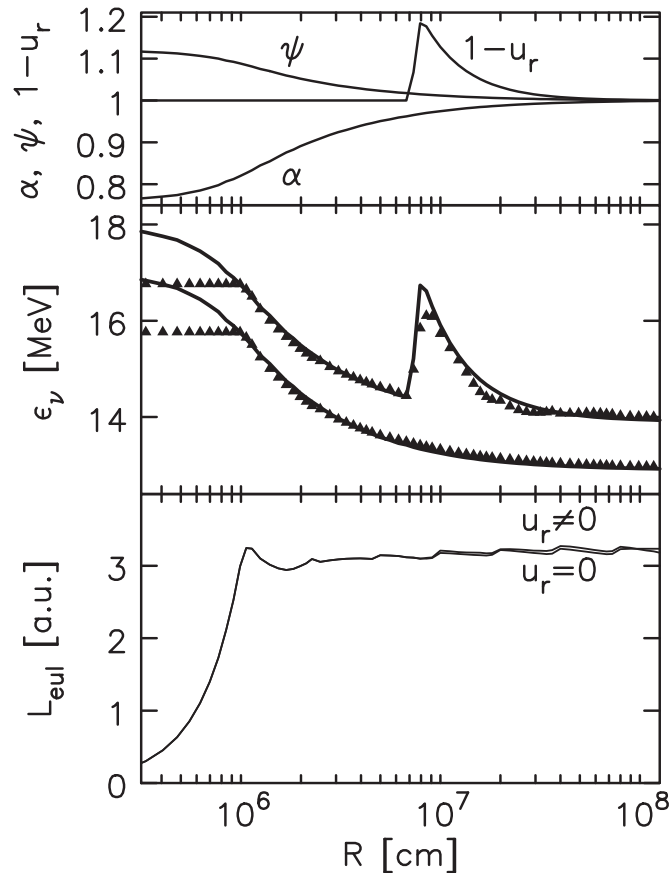


Figure 6. In the top panel, we show background profiles for ψ , α , and $1 - u_r$. The mean energy (ϵ) and Eulerian luminosity L_{eul} profiles are plotted in the middle and bottom panels, respectively. Two test cases, with ($u_r \neq 0$) and without ($u_r = 0$) the shock profile, in the curved spacetime are plotted. In the middle panel, our results are denoted by filled triangles and the solid lines are analytical results. Note that $\langle \epsilon \rangle$ for the model with the shock profile is shifted upward with 1 MeV to avoid the overlapping of plots.

$$\sqrt{\gamma} \alpha r^2 \gamma^{rr} \int d\epsilon F_r \equiv L_{\text{eul}} = \text{const}, \quad (69)$$

where W is the Lorentz factor, and $v_r = u_r/u^t$. $\sqrt{\gamma} = \psi^6$ and $\gamma^{rr} = \psi^{-4}$ are the determinant and rr -component of the three metrics, respectively, in the conformally flat approximation. L_{eul} is the luminosity measured by an Eulerian observer. Equation (69) is derived from the stationary solution of Equation (4) with neglecting the source terms.

In the top panel of Figure 6, we show the background profiles for ψ , α , and $1 - u_r$. $\langle \epsilon \rangle$ and L_{eul} are plotted in the middle and bottom panels, respectively. In the middle panel, our results (filled triangles) and analytical ones (solid lines) are plotted. The analytical expression for $\langle \epsilon \rangle$ is derived from Equation (68), where the constant in the rhs is evaluated at $R = 10$ km. Numerical results are taken after they settle down in nearly stationary.

As seen in the middle panel, our results reproduce the analytical ones quite well except at the shock front. We consider that the less agreement at the shock front originates from the coarse spatial resolution. The finite difference expression for the term $\nabla_\alpha u_\beta$ in the energy-coupling terms cannot capture the sharp velocity profile with enough accuracy. From the bottom panel, we can find the Eulerian luminosity stays nearly constant with a few percent deviation beyond

$R \gtrsim 20$ km. Note that the zig-zag pattern seen in L_{eul} is an artifact of the mesh refinement.

5. CORE COLLAPSE OF A $15M_\odot$ STAR

In order to confirm the validity of our new supernova code, it is of primary importance to make a detailed comparison with the previously published results. We employ the data from 1D-GR neutrino transport simulations (Liebendörfer et al. 2005; Sumiyoshi et al. 2005; Müller et al. 2010) and from 2D-GR ones (Müller & Janka 2014). We chose these models because all of them took the same progenitor and employed similar microphysics in the GR CCSN simulations. Liebendörfer et al. (2005) presented detailed comparison of two independent numerical codes, AGILE-BOLTZTRAN (Liebendörfer et al. 2004) and VERTEX-PROMETHEUS (Rampp & Janka 2002). Since their results are available online⁹, we are able to make a detailed comparison with their data set. AGILE-BOLTZTRAN solves the GR Boltzmann equation with the S_n method in spherically symmetric Lagrangian mesh, whereas VERTEX is an Eulerian code that solves the moment equations of a model Boltzmann equation by the VEF method in the Newtonian hydrodynamics plus a modified GR potential (VERTEX-PROMETHEUS) and also in the conformally flat GR hydrodynamics (VERTEX-CoCoNuT; Dimmelmeyer et al. 2002; Müller et al. 2010). Our code is rather similar to VERTEX-CoCoNuT than AGILE-BOLTZTRAN except for the different geometrical solvers and the different coordinate systems are adopted. In the following, we label the results of AGILE-BOLTZTRAN as “ABG15,” of VERTEX-PROMETHEUS as “VXG15,” and of Müller et al. (2010) as “BMG15.”¹⁰

5.1. Numerical Setups

We employ a $15M_\odot$ progenitor (model “s15s7b2” in Woosley & Weaver 1995) and follow core-collapse, bounce, and initial postbounce phase up to ~ 50 ms. We use the EOS of Lattimer & Douglas Swesty (1991; LS EOS) with an incompressibility parameter of $K = 220$ MeV. Even though our choice of $K = 220$ MeV is different from the one ($K = 180$ MeV) used in Liebendörfer et al. (2005), Sumiyoshi et al. (2005), Müller et al. (2010), Müller & Janka (2014), and Thompson et al. (2003) showed that differences in the neutrino profiles among models with the different K of LS EOS are a few percent around core bounce and less than $\sim 10\%$ for the first ~ 200 ms after bounce. We thus consider that the different choice of K barely disturbs the aim of our comparison study.

As for neutrino opacities, the standard weak interaction set in Bruenn (1985) and Rampp & Janka (2002) plus nucleon–nucleon bremsstrahlung (Hannestad & Raffelt 1998) is taken into account (see Table 1 and Appendix A for more details). For simplicity, we neglect higher harmonic angular dependence of the reaction angle when we calculate the source terms for neutrino electron scattering, thermal pair production, and the annihilation of neutrinos, and nucleon–nucleon bremsstrahlung (i.e., $B_{(\epsilon),\text{nes/tp}}^{0,\mu}$ and $C_{(\epsilon),\text{nes/tp}}^{1,\mu}$ are set to be 0; see Appendices A.3 and A.4).

In this study, we investigate two models, 1DG15 and 3DG15, both of which are computed in the 3D Cartesian

⁹ We used data which can be downloaded at <http://iopscience.iop.org/0004-637X/620/2/840/fulltext/datafiles.tar.gz>.

¹⁰ We read their data from the figures digitally and plot them in this paper.

Table 1
The Opacity Set Included in this Study and their References

Process	Reference	Summarized In
$\nu\nu_e \leftrightarrow e^-p$	Bruenn (1985), Rampp & Janka (2002)	Appendix A.1
$p\bar{\nu}_e \leftrightarrow e^+n$	Bruenn (1985), Rampp & Janka (2002)	Appendix A.1
$\nu_e A \leftrightarrow e^-A'$	Bruenn (1985), Rampp & Janka (2002)	Appendix A.1
$\nu p \leftrightarrow \nu p$	Bruenn (1985), Rampp & Janka (2002)	Appendix A.2
$\nu n \leftrightarrow \nu n$	Bruenn (1985), Rampp & Janka (2002)	Appendix A.2
$\nu A \leftrightarrow \nu A$	Bruenn (1985), Rampp & Janka (2002)	Appendix A.2
$\nu e^\pm \leftrightarrow \nu e^\pm$	Bruenn (1985)	Appendix A.3
$e^-e^+ \leftrightarrow \nu\bar{\nu}$	Bruenn (1985)	Appendix A.4
$NN \leftrightarrow \nu\bar{\nu}NN$	Hannestad & Raffelt (1998)	Appendix A.5

Note. Note that ν , in neutral current reactions, represents all species of neutrinos ($\nu_e, \bar{\nu}_e, \nu_x$) with ν_x representing heavy lepton neutrinos (i.e., ν_μ, ν_τ and their anti-particles).

coordinates. While model 3DG15 is calculated without any artificial constraints, model 1DG15 is considered to mimic the 1D model by artificially suppressing the non-radial component of the flow velocity u_i as

$$u_i = \frac{x^j u_j}{|x|^2} x^i. \quad (70)$$

Although this artificial elimination could potentially lead to a shift of the kinetic energy into the thermal one, our previous study (Kuroda et al. 2012) showed that the violation of the momentum constraint is negligible during the early postbounce phase ($T_{\text{pb}} \lesssim 100$ ms where T_{pb} denotes the postbounce time).

The 3D computational domain is a cubic box with 8000 km width (i.e., the outer boundary is at the radius of 4000 km from the origin) and nested boxes with 5 refinement levels, at the beginning of calculation, to 8 refinement levels, when the central rest mass density reaches 5×10^{13} g cm $^{-3}$, are embedded without any spatial symmetry. Each box contains 64^3 cells and the minimum grid size near the origin at bounce is $\Delta x = 488$ m. In the vicinity of the stalled shock front $R \sim 100$ km, our resolution achieves $\Delta x \sim 3.6$ or 7.2 km, i.e., the effective angular resolution becomes 3.6 km/100 km $\sim 2^\circ$ or $\sim 4^\circ$, which is considered to be a rather too coarse resolution to follow a nearly spherical structure in the Cartesian grids. Compared to recent 3D-GR studies (Ott et al. 2012; Kuroda et al. 2014), the resolution is still approximately two times coarser. The time step size is $\Delta t = 10^{-7}$ s which corresponds to ~ 0.06 in the CFL number. The main reason for taking such a small time step is to get a rapid convergence during the iteration in our implicit time update part (see Section 3.3), which is not restricted by the CFL condition (of the explicit update in a pure hydrodynamics case). As for the energy grid of the neutrino radiation field, we use logarithmically spaced 20 energy bins ($N_\varepsilon = 20$) which center from $\varepsilon = 1$ to 300 MeV.

5.2. Results

In this section we start to make a detailed comparison first before bounce (Section 5.2.1) and then after bounce (Section 5.2.2) between our code (models 1DG15 and 3DG15), AGILE-BOLTZTRAN (model ABG15), VERTEX-PROMETHEUS (model VXG15), and (partly) from VERTEX-COCONUT (model BMG15). In the following, we call the results from the latter three codes the *reference* results.

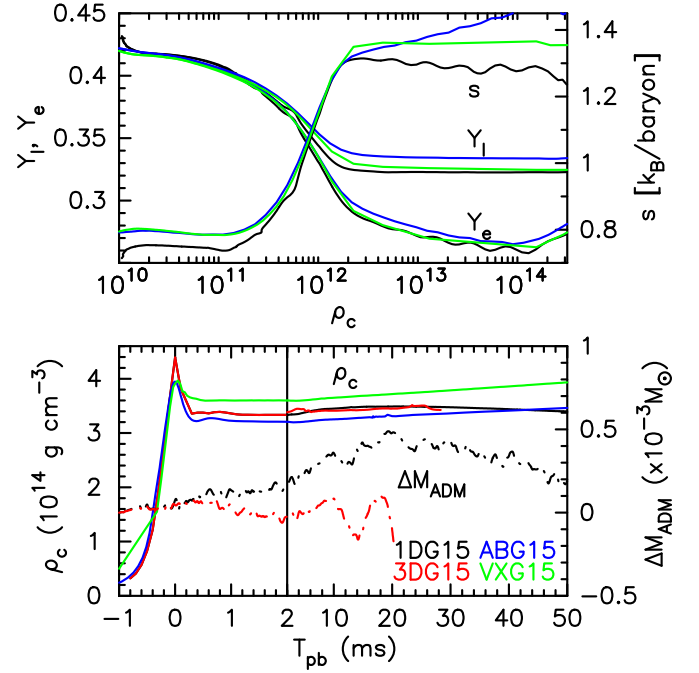


Figure 7. Upper panel: the central (matter) entropy s , electron fraction Y_e , and total lepton fraction $Y_l = Y_e + Y_n$ as a function of central density ρ_c for model 1DG15 (black), ABG15 (blue), and VXG15 (green). Lower panel: comparison of postbounce evolution of the central density (solid) between the four models and the deviation of the ADM mass ΔM_{ADM} (dashed-dotted) for our two models with (model 1DG15) or without the artificial elimination of the non-radial velocity (model 3DG15; see the text).

5.2.1. Before Bounce

In the upper panel of Figure 7, we plot the central (matter) entropy s , electron fraction Y_e , and the total lepton fraction $Y_l = Y_e + Y_n$ as a function of the central (rest mass) density ρ_c for model 1DG15 (black), ABG15 (blue), and VXG15 (green), respectively. The lower panel of Figure 1 shows the evolution of ρ_c and the deviation of the ADM mass ΔM_{ADM} from its initial value. Here M_{ADM} is given by

$$M_{\text{ADM}} = \int dx^3 \left[\left(S_0 + \int d\varepsilon E_{(\nu, \varepsilon)} \right) e^{-\phi} + \frac{e^{5\phi}}{16\pi} \left(\tilde{A}_{ij} \tilde{A}^{ij} - \frac{2}{3} K^2 - \tilde{\gamma}^{ij} \tilde{R}_{ij} e^{-4\phi} \right) + \int d\sigma \left[e^{-\phi} \left(S^i + \int d\varepsilon F_{(\nu, \varepsilon)}^i \right) \cdot \hat{n} \right], \quad (71)$$

where the second line denotes energy loss due to momentum and neutrino energy flux through the numerical boundary and \hat{n} represents a unit normal vector to the surface element $d\sigma$. In the above surface integration, we neglect energy loss due to gravitational wave emission since it is negligibly small ($\sim 10^{-11} M_\odot c^2$; e.g., Scheidegger et al. 2010) compared to the violation of the ADM mass in the CCSN environment (see, e.g., Kotake 2013 for a review).

The top panel of Figure 1 shows that the neutrino trapping starts $\rho_c \sim 2 \times 10^{12}$ g cm $^{-3}$ for model 1DG15 and the lepton fraction remains constant with $Y_l = 0.323$ afterward. The evolution of our central Y_e and Y_l (black lines) is quantitatively in good agreement with VXG15 (green line; see also Buras et al. 2006b; Müller et al. 2010) and ABG15 (blue line). As

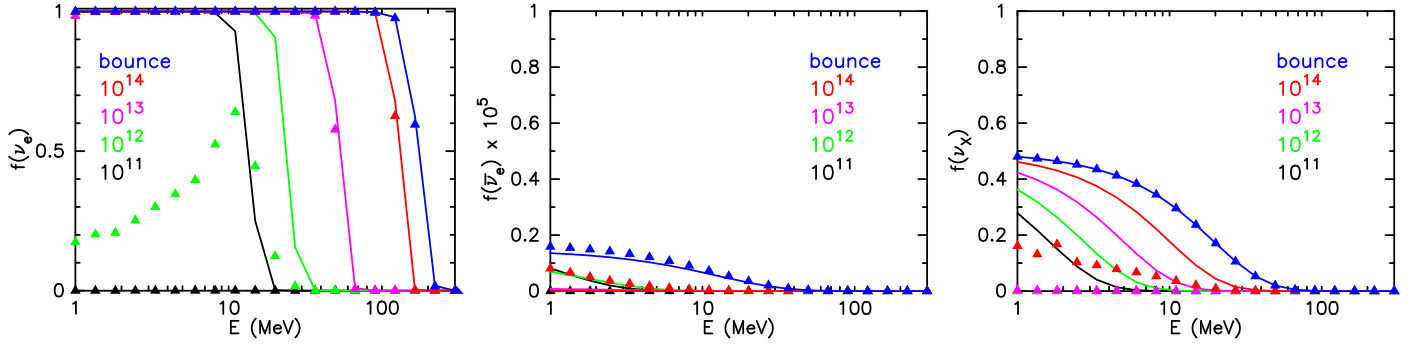


Figure 8. Neutrino distribution function $f(\nu, \varepsilon)$ (filled triangles) and Fermi–Dirac distribution function at equilibrium (solid lines) at the innermost mesh for model 1D-GR. Lines and triangles are color coded according to the infall phase. Note that $f(\nu, \varepsilon)$ for anti-electron neutrino ($\bar{\nu}_e$) is multiplied by 10^5 for comparison.

already explained in Section 2.2, we solve the advection equation (Equation (20)) of the total lepton number (density) ρY_l as a constraint to ensure the lepton number conservation. Because of the treatment, the evolution of the lepton/electron fraction is in excellent agreement with the reference results. As already pointed out by O’Connor (2014), this also relies on the accurate implementation of inelastic neutrino–electron scattering, energy–bin coupling, and the appropriate closure relation.

After the core deleptonization ceases (i.e., Y_l stays nearly constant with increasing central density), the inner core evolves almost adiabatically and the entropy remains nearly constant as it should be. A small breaking of the adiabaticity (decrease by 3.8% in the central entropy) is seen in model 1DG15 before bounce (see also O’Connor 2014). However, the (time-averaged) value $s \sim 1.3 k_B \text{ baryon}^{-1}$ is in roughly good agreement with the reference results (see also Liebendörfer et al. 2005; Sumiyoshi et al. 2005; Buras et al. 2006b; Müller et al. 2010) and this would not have a big impact on the subsequent core evolution due to the short simulation time in this study.

As for the total energy conservation (bottom panel of Figure 3), it is maximally violated with the amount of $\Delta M_{\text{ADM}} \sim 4 \times 10^{-4} M_\odot$ for model 1DG15 (i.e., $\sim 8 \times 10^{50}$ erg). The violation at bounce is slightly worse than that ($\Delta_{\text{ADM}} \sim 5 \times 10^{50}$ erg) of the VERTEX-CoCoNut code (Müller et al. 2010), which should be improved and kept much smaller in more precise CCSN modeling. As one would anticipate, the violation is bigger for model 1DG15 (dashed black line) with the artificial elimination of the non-radial velocity than for model 3DG15 without (dashed red line). In our previous study (with the gray M1 scheme; Kuroda et al. 2012), the violation of the ADM mass is typically one order of magnitude smaller than that for the corresponding 3D model with (approximately) twice higher resolution. Because the computational time for the implicit update in the current code is very expensive (using our best available resources), we are now forced to employ a quite coarse resolution. It is important to clarify how the violation of the total energy conservation would be improved with increasing numerical resolution. We leave this for future work.

Figure 8 shows a spectral shape of the neutrino distribution function $f(\nu, \varepsilon)$ (filled triangles),

$$f(\nu, \varepsilon) = \frac{J_{(\nu, \varepsilon)}}{4\pi\varepsilon^3}, \quad (72)$$

which is estimated at the innermost grid point of model 1DG15 when the central density ρ_c reaches $10^{11,12,13,14} \text{ g cm}^{-3}$, and at bounce, respectively. Solid curves represent the Fermi–Dirac distribution at equilibrium. From the left panel, it can be seen that β -equilibrium is achieved for electron-type neutrino (ν_e) at $10^{12} \text{ g cm}^{-3} \lesssim \rho_c \lesssim 10^{13} \text{ g cm}^{-3}$, which is consistent with the neutrino trapping density as shown in Figure 7. In Bruenn (1985), the β -equilibrium for ν_e was obtained after $\rho_c = 2.46 \times 10^{12} \text{ g cm}^{-3}$ in their model that corresponds to ours (“standard” model). Note that at bounce, electron-type neutrinos, in the low-energy range $\lesssim 5 \text{ MeV}$, slightly violate the Fermi blocking, i.e., the distribution function $f(\nu_e)$ exceeds one. The excess, however, is $\lesssim 10^{-5}$ and we consider that it is a negligible amount. As shown from the middle ($\bar{\nu}_e$) and right panels (ν_χ) of Figure 4, other neutrino species are thermalized only after ρ_c exceeds $10^{14} \text{ g cm}^{-3}$. These features are quantitatively consistent with Bruenn & Mezzacappa (1997) and Rampp & Janka (2002). It may be surprising that regardless of the use of different EOS and different hydrodynamics codes, the trapping density of ν_e ($\rho_{\text{trap}} = 2 \sim 3 \times 10^{12} \text{ g cm}^{-3}$) in modern simulations (e.g., top panel of Figure 3) is in good agreement with the pioneering work in the 1980s (Bruenn 1985). It should be also noted that for the more accurate determination of the core deleptonization the improved electron capture rates (Langanke & Martínez-Pinedo 2000; Juodagalvis et al. 2010) need to be implemented as in Langanke et al. (2003) and Lentz et al. (2012a, 2012b).

So far, we have shown that our M1 scheme can capture several important phenomena regarding deleptonization, such as the neutrino trapping and the conservation of the lepton fraction in the diffusion region. As already denoted in Section 2.1, this is not trivial in the finite difference method especially when one transports conservative radiation moments ($E_{(\varepsilon)}$, $F_{(\varepsilon)i}$) instead of the corresponding comoving variables of ($\mathcal{J}_{(\varepsilon)}$, $\mathcal{H}_{(\varepsilon)i}$). A key is finding an appropriate Eddington factor $\chi_{(\varepsilon)}$ by which the neutrino energy flux approaches $F_{(\varepsilon)}^i \rightarrow 4/3 E_{(\varepsilon)} v^i$ in the diffusion limit (see Equation (26)). Since this relation can be achieved only when $P_{(\varepsilon)}^{ij} = E_{(\varepsilon)} \gamma^{ij}/3$ holds, $\chi_{(\varepsilon)}$ and \bar{F} should approach 1/3 and 0 (e.g., our closure relation (Equation (6)) in the limit, respectively).

To show that both $\bar{F} = \sqrt{h_{\mu\nu} H_{(\varepsilon)}^\mu H_{(\varepsilon)}^\nu} / J_{(\varepsilon)}^2$ and $F_{(\varepsilon)}^i$ actually approach 0 and $4/3 E_{(\varepsilon)} v^i$ in the opaque region, we plot in Figure 9 the radial profiles of $\langle F_r \rangle / \langle E \rangle$ (solid lines) and $\langle H_r \rangle / \langle J \rangle$

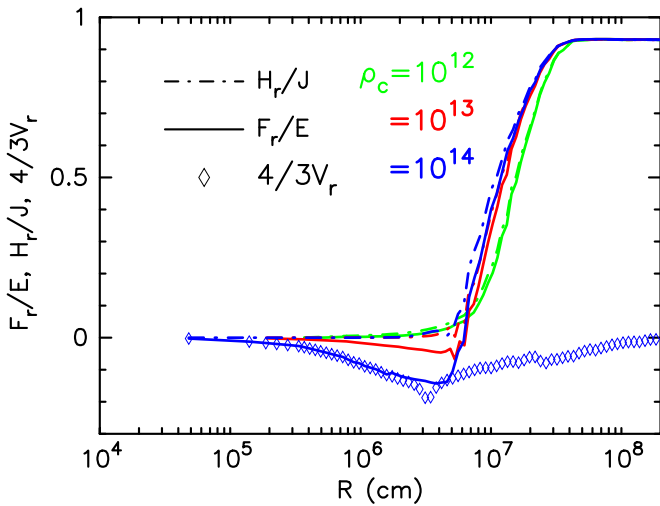


Figure 9. Radial profiles of $\langle F_r \rangle / \langle E \rangle$ (solid lines) and $\langle H_r \rangle / \langle J \rangle$ (dashed–dotted lines) for electron-type neutrino (ν_e) when the central density reaches $\rho_c = 10^{12,13,14} \text{ g cm}^{-3}$ in model 1DG15. V_r denotes the radial velocity of matter (see the text).

(dashed–dotted lines) at different ρ_c . Here $\langle X \rangle \equiv \int d\epsilon X$ represents the energy integration of X . At $\rho_c = 10^{12} \text{ g cm}^{-3}$, both solid and dashed–dotted green lines almost coincide. However, as the infalling matter velocity comes closer to being relativistic ($\rho_c \gtrsim 10^{13} \text{ g cm}^{-3}$), both lines start to split especially within $R \gtrsim 70 \text{ km}$. In the central region ($R \lesssim 70 \text{ km}$), $\langle H_r \rangle / \langle J \rangle$ approaches 0 toward the center, whereas $\langle F_r \rangle / \langle E \rangle$ becomes negatively large with the peak being around $R \sim 30 \text{ km}$ and then converges to zero to the center. We also plot the radial velocity of matter (V_r) measured in the Eulerian frame and multiplied by 4/3 (blue diamonds) at $\rho_c = 10^{14} \text{ g cm}^{-3}$.

Because of our appropriate evaluation for the Eddington factor, the flux factor measured in the Eulerian frame (approximated here by $\langle F_r \rangle / \langle E \rangle$) nicely matches with $4V_r/3$ in the optically thick region. This neutrino advection is essentially important for the radiation energy ($E_{(e)}$) to move with the same velocity v^i with matter in the opaque region (see Equations (26)–(29)). Here we shortly comment on the definition of the flux factor \bar{F} . In our previous study (Kuroda et al. 2012), we employed the definition $\bar{F} \equiv \sqrt{\gamma^{\bar{i}\bar{j}} F_{\bar{i}} F_{\bar{j}} / E}$, which is one of the candidates for \bar{F} (Shibata et al. 2011). As can be clearly seen from the split between the solid and dashed–dotted lines in Figure 9, we show that our previous choice of the flux factor is not adequate because the optically thick medium moves (albeit mildly) relativistically in the collapsing core.

5.2.2. After Bounce

In Figure 10, we show the radial profiles of various quantities (the rest mass density ρ , radial velocity v_r , matter temperature T , entropy s , averaged neutrino energy E_ν , and electron/neutrino fraction Y_e/Y_l) at the selected time slices shortly after bounce. Here, we define the average neutrino energy E_ν as

$$E_\nu \equiv \frac{\int d\epsilon \epsilon^3 f(\nu, \epsilon)}{\int d\epsilon \epsilon^2 f(\nu, \epsilon)}. \quad (73)$$

When the central density exceeds nuclear saturation densities (top left panel of Figure 10), the core bounces because of the

strong repulsive force of nuclear matter. Then the bounce shock is formed (green line, left middle panel of Figure 10) which propagates outward with dissociating infalling heavy nuclei into free protons and neutrons. The production of enormous free protons/neutrons significantly enhances the electron capture process, $e^-p \rightarrow \nu_e n$, behind the stalling shock. Immediately after bounce, those high-energy neutrinos (top right panel) are still trapped inside the optically thick medium behind the shock. The medium, however, quickly becomes transparent to neutrinos and those neutrinos are liberated suddenly as a burst. This neutronization burst enhances further electron capture behind the shock due to the continuous deviation from the β -equilibrium, leading to a characteristic trough in the Y_e profile seen at $R \sim 50 \text{ km}$ behind the shock (right bottom panel of Figure 10). Due to the energy loss by the photodissociation of the iron nuclei and the rapid neutrino leakage, the bounce shock stalls at $R \sim 70 \text{ km}$ within $T_{\text{pb}} \sim 3 \text{ ms}$ (left panels of Figure 10). Such dynamical features are commonly seen in the reference models (Liebendörfer et al. 2005; Müller et al. 2010). This indicates that our MI scheme can capture the basic behaviors of the neutrino propagation from the optically thick to thin medium (otherwise it would result in either the absence or the different position of the Y_e trough).

How the neutronization burst is produced is more clearly depicted in Figure 11 where we plot the radial profiles of the neutrino (ν_e) energy flux (solid lines) and the radial velocity of matter (dashed–dotted lines). At $T_{\text{pb}} = 0.7 \text{ ms}$, enormous neutrinos are still trapped and confined behind the shock, which is shown as a sharp peak in the energy flux around $10 \lesssim R \lesssim 20 \text{ km}$. At $T_{\text{pb}} = 1.7 \text{ ms}$, these neutrinos overtake the shock front because of the lowering opacity outward. Then the pulse of the neutrino burst propagates freely to the optically thin region (time label larger than 4) and eventually emerges out of the computational domain (labels 9 and 10). These profiles are consistent with the results of Bruenn & Haxton (1991), Thompson et al. (2003), and Rampp & Janka (2002).

Now we move on to make the code comparison in the postbounce phase. Figure 12 compares the evolution of the shock radii for five models; two from our code (1DG15 (black line) and 3DG15 (red line)), one from AGILE-BOLTZTRAN (ABG15, blue line), and two from VERTEX with PROMETHEUS (VXG15, green line) and with CoCoNuT (BMG15, light blue line). Note that the final simulation time (T_{sim}) is 50 ms for model 1DG15 (black line), whereas T_{sim} is 32 ms for model 3DG15 (red line) simply limited by our available computational resources.

The deviation seen in model 3DG15 (red line in Figure 12) from the rest of the 1D models is remarkable especially after $T_{\text{pb}} \sim 5 \text{ ms}$. This is because the bounce shock expands more energetically in 3D pushed primarily by prompt convection behind the shock. Using the same progenitor, Müller et al. (2012b) showed that the average shock radius becomes larger in 2D (their model G15) than in 1D (their model G15–1D) at $T_{\text{pb}} \sim 70 \text{ ms}$ because of the hot-bubble convection starts which is seeded during the deceleration of the prompt shock. The Cartesian coordinates have intrinsic quadrupole perturbation and it significantly affects the growth of the prompt convection. The postbounce time, when the significant multidimensionality appears, thus differs between our model and the ones using the spherical polar coordinates. In addition, our coarse numerical

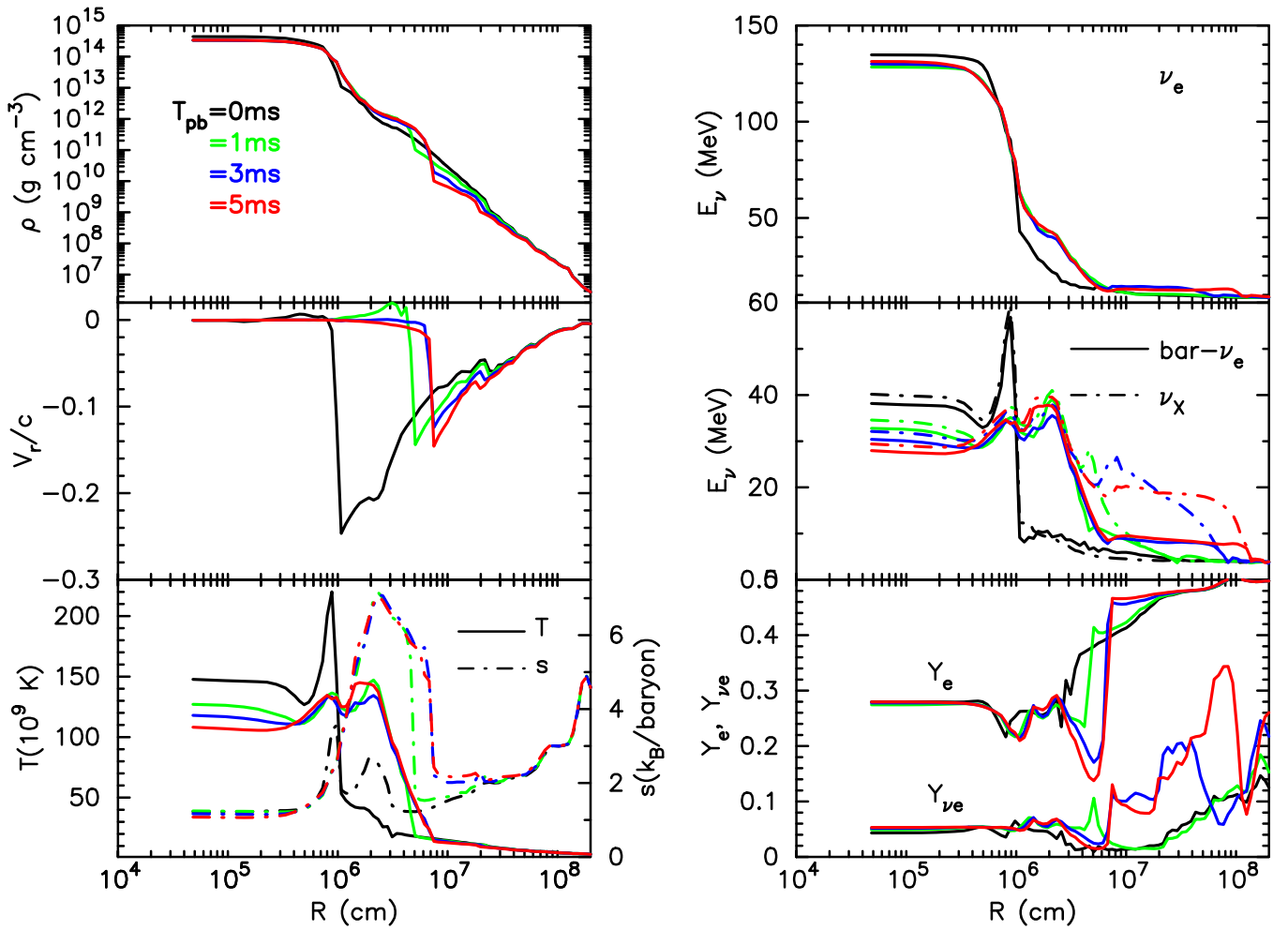


Figure 10. Radial profiles of the rest mass density ρ , the radial velocity v_r normalized by the speed of light c , the matter temperature T , the entropy s , the averaged neutrino energy E_ν , and the electron/neutrino fractions Y_e/Y_ν at selected time slices shortly after bounce $T_{\text{pb}} = 0, 1, 3,$ and 5 ms. Note in this plot that profiles only along the x -axis of model 1DG15 are shown (because model 3DG15 shows almost the same profiles).

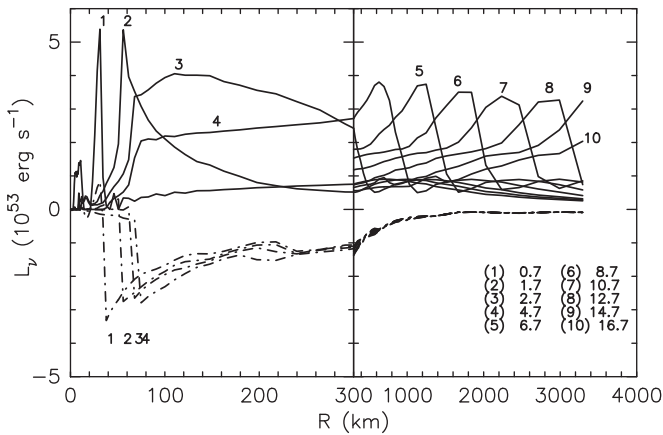


Figure 11. Radial profiles of the (electron-type) neutrino energy flux (solid lines) and the radial velocity (dashed-dotted lines). The numbers beside each line (1, 2, 3...) correspond to time slices, which are denoted in the lower right with T_{pb} in ms (0.7, 1.7, 2.7...). For the radial velocity in the left panel, we plot only the first four time slices.

resolution might also lead to the earlier appearance of the initial convection because of even larger seed perturbations.

The larger shock radius in model 3DG15 than that in 1DG15 is also consistent with our previous result with the leakage

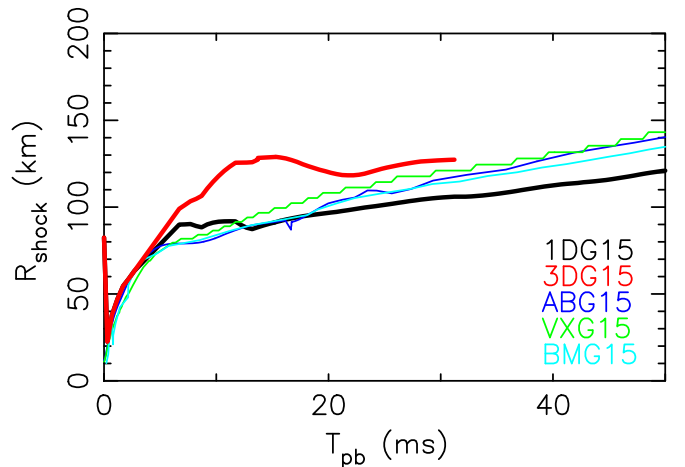


Figure 12. Time evolution of the shock radius for five different models 1DG15, 3DG15, ABG15, VXG15, and BMG15. As for our models, we plot the angle-averaged values.

scheme (Kuroda et al. 2012; see also Hanke et al. 2012; Couch 2013 for extensive discussions about the dimensional dependence on the postbounce dynamics). Now let us focus on our (pseudo-) 1D model (black line in Figure 12). The shock radius

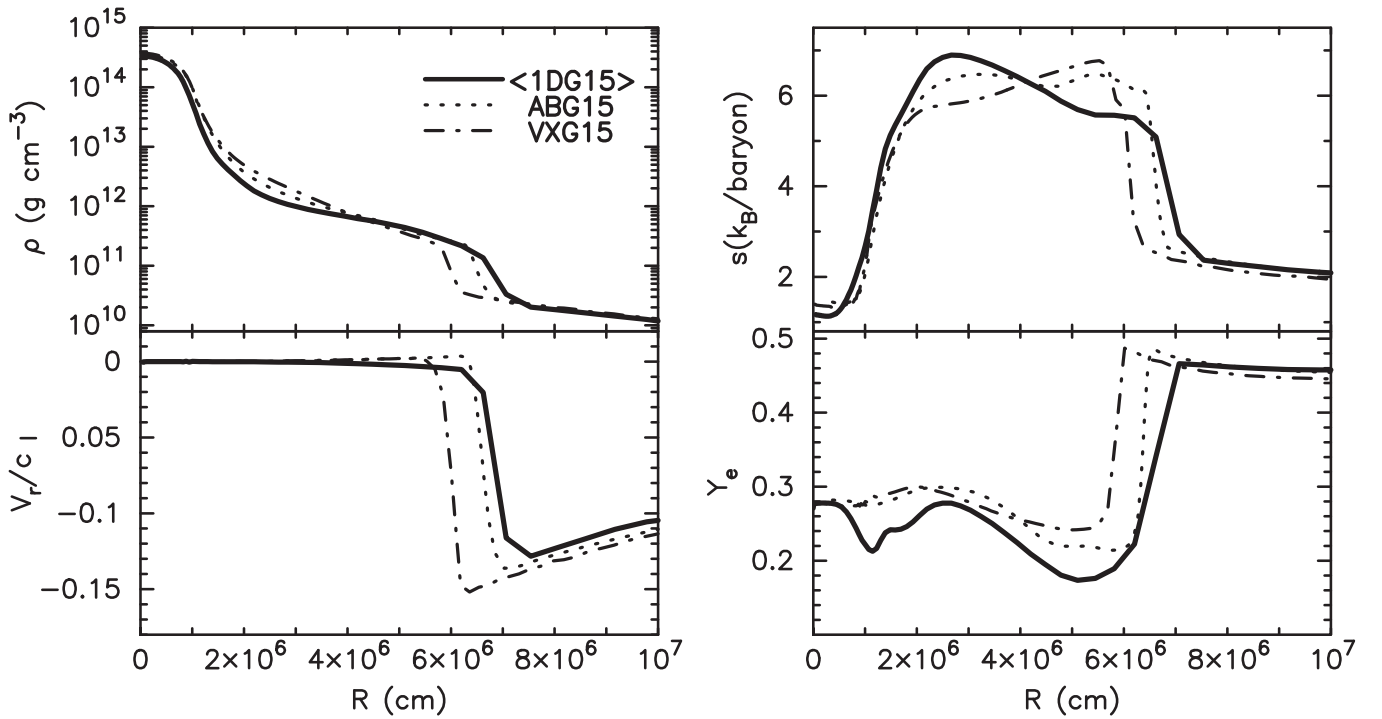


Figure 13. In the clockwise direction from the top left panel, we show radial profiles of the (angle-averaged) rest mass density ρ , entropy s , electron fraction Y_e , and radial velocity V_r at $T_{\text{pb}} = 3$ ms for models “(1DG15),” “ABG15,” and “VXG15.”

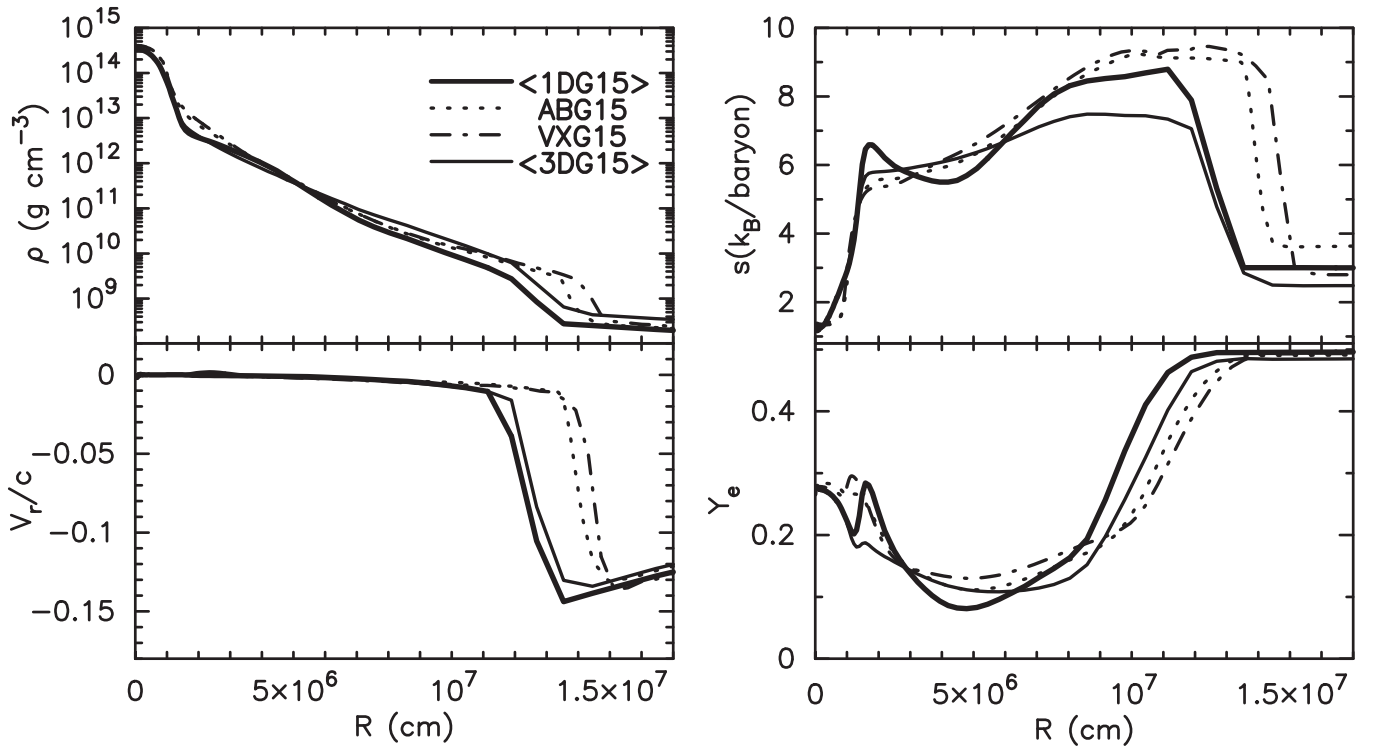


Figure 14. Same as Figure 13, but at $T_{\text{pb}} = 50$ ms for models “(1DG15),” “ABG15,” and “VXG15.” “(3DG15)” at $T_{\text{pb}} = 32$ ms is also plotted as a reference by a thin solid line.

of our code is in good agreement with the reference results exceptionally before $T_{\text{pb}} \lesssim 20$ ms, whereas the shock radius tends to be smaller until the end of the simulation time. We consider that the difference could primarily come from the use of the Cartesian coordinates with low numerical resolution and not from the neutrino–matter interaction terms. This is because

our calculation in 1D spherical coordinates with using the same neutrino–matter interaction terms shows a good agreement in the shock evolution (see Appendix B). We give a more detailed discussion elsewhere below.

In Figures 13 and 14, we show various quantities from our code (labeled by “(1DG15)” and “(3DG15)” only in Figure 14),

AGILE-BOLTZTRAN (“ABG15”), and VERTEX-PROMETHEUS (“VXG15”) at two different postbounce times.

At 3 ms after bounce (Figure 13), the (angle-averaged) radial position of the stalled shock (bottom left panel) is $R \sim 70$ km for model 1DG15 (thick solid line). As seen, the velocity profile matches more closely the profile from AGILE-BOLTZTRAN (ABG15) than from VERTEX-PROMETHEUS (VXG15). This is also the case for the profiles of the density (top left panel), entropy (top right panel), and Y_e (bottom right panel). It should be noted that the more recent results from the VERTEX-PROMETHEUS code with an improved GR potential (Marek et al. 2006) agree very well with the AGILE-BOLTZTRAN code, hence with our code. Therefore, we mainly compare to model ABG15 in the following.

Looking at Figure 13 more closely, one can see that the profiles of our entropy (top right panel) and Y_e (bottom right panel) differ appreciably from model ABG15 especially in the region behind the stalled shock ($R \lesssim 70$ km) and above the unshocked inner core ($R \gtrsim 10$ km). Let us remark that the early postbounce evolution starts from the shock formation, followed by the emergence of the neutronization burst, until the shock stall is numerically most challenging. The code differs from the shock-capturing scheme as well as the treatment of GR, and the accuracy of the neutrino transport schemes could potentially impact the radiation-hydrodynamics evolution at the transient phase (i.e., 3–5 ms after bounce). Another remarkable difference is seen in the electron fraction. Among three results, only our result shows negative bump in Y_e profile at $10 \lesssim R \lesssim 20$ km. However, this bump disappears in our 1D spherically symmetric test problem in which we solve the advection terms in energy space $\mathcal{S}_{\text{adv},e}$ explicitly in time (see Appendix B for more details).

Regarding the shock capturing, AGILE-BOLTZTRAN uses an artificial viscosity type with the second order accuracy in space, whereas our code employs the approximate Riemann solver (HLLC scheme like the VERTEX code) with second-order accuracy in space for both radiation-hydrodynamical and geometrical variables. Thus, the hydrodynamics part of our code is slightly more accurate than AGILE-BOLTZTRAN. On the other hand, the use of the approximate closure relation apparently falls behind the Boltzmann code especially in the semi-transparent region. Above all, the use of the Cartesian coordinates, which is very common in full GR simulations,¹¹ makes the comparison to the genuine “1D” results of the reference models (based on the 1D Lagrangian code (AGILE) and the multi-D code using the polar coordinates (VERTEX)) even more challenging.

At $T_{\text{pb}} = 50$ ms (Figure 14), the differences between our pseudo-1D model (1DG15, thick line) and the reference results still remain to be seen rather remarkably in the postshock region ($R \gtrsim 100$ km); however, this is not surprising given the different shock evolution (Figure 12). Here we consider that the numerical resolution in the postshock region sensitively affects the shock evolution. In the current resolution, the typical grid size of our nested box is ~ 7.8 km at $120 \lesssim R \lesssim 240$ km ($\sim 4^\circ$ resolution). As shown in Figure 12 (red line), the deviation of the shock radius from the reference models becomes remarkable at $T_{\text{pb}} \gtrsim 20$ ms, which roughly coincides with the time when the shock reaches the coarser level of the nested grid. There the shock front is resolved only by a few grid cells. We

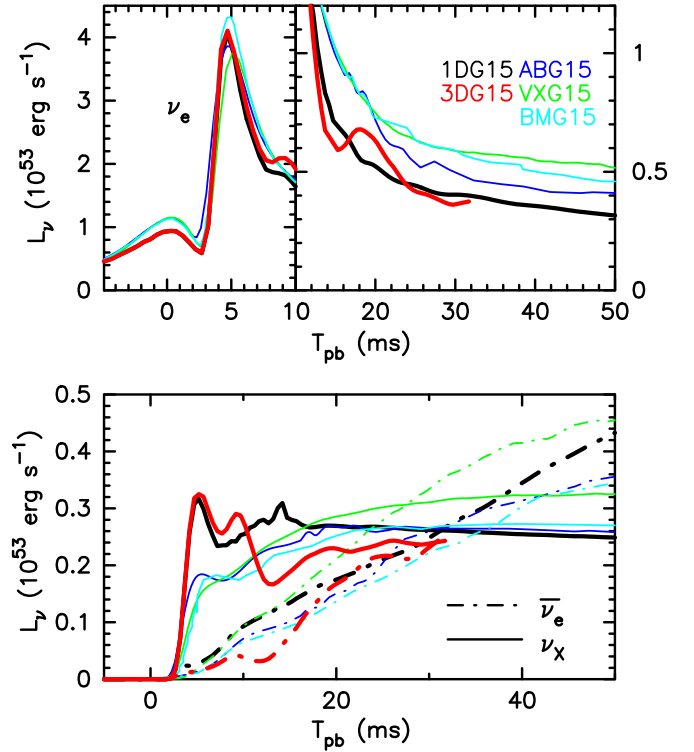


Figure 15. Same as Figure 12 but for the neutrino luminosity L_ν of electron-type neutrinos (top panel) and anti-electron-type and heavy-type neutrinos (bottom panel) for the five different models.

consider that at least a factor of two or more higher resolution is required to reproduce 1D results, i.e., to recover the sphericity of the system in the Cartesian coordinates. However, this is not an easy task as we will discuss the code performance in Section 6.

From Figure 14, one can also see that the profile of the density, velocity, entropy, and Y_e at the central region ($R \lesssim 60$ km) agrees with the reference results roughly within an accuracy of $\sim 10\%$. Given the insufficient numerical resolution, this good agreement in the semi-transparent region would support the validity of the prescribed closure scheme, which is in line with the recent results by O’Connor (2014) and Just et al. (2015). Figure 14 also shows that the profile of model 3DG15 (thin solid line) differs from that of model 1DG15 (thick solid line).

The entropy profile for model 3DG15 (thin line) behind the shock ($R \lesssim 130$ km) becomes flatter compared to the 1D models, which is due to convective mixing behind the shock. As a result, the profiles of Y_e and entropy in model 3DG15 become slightly closer to the reference results, though the similarity is just a coincidence and is not meaningful.

Figure 15 shows the comparison of the neutrino luminosity L_ν , which is the surface integral of the energy-integrated comoving energy flux $H_{(e)}^\mu$ through the surface of cubic box with 1000 km width (i.e., approximately 500 km from the origin). The peak luminosity, $L_{\nu_e, \text{peak}} = 4.1 \times 10^{53}$ erg s $^{-1}$, well agrees with 3.85×10^{53} (ABG15), 3.8×10^{53} (VXG15), and 4.3×10^{53} (BMG15), respectively. After the neutronization phase when the 1D core enters to a quasi-static phase ($T_{\text{pb}} \gtrsim 20$ ms), the anti-electron and heavy lepton neutrino luminosities show quite consistent behaviors with the reference

¹¹ See, however, Sanchis-Gual et al. (2014) for a recent report of the code development of numerical relativity in the polar coordinates.

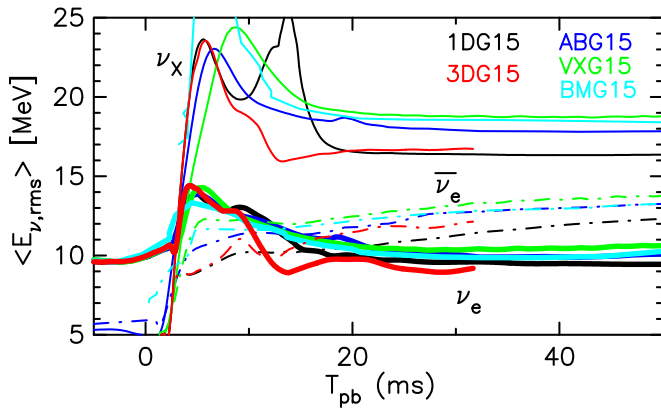


Figure 16. Time evolution of rms energies of emergent neutrinos $E_{\nu, \text{rms}}$ for five different models. Our results are measured at the surface of cubic box with 1000 km width.

models and the differences between our results and, e.g., ABG15 are as small as $\sim 10\%$.

Regarding the ν_e luminosity, we see a systematically lower value than the other three reference models. The difference reaches $\sim 30\%$ (or $\sim 10^{52} \text{ erg s}^{-1}$) compared to ABG15 at $T_{\text{pb}} = 50 \text{ ms}$. As a consequence, ν_e and $\bar{\nu}_e$ luminosities become comparable at $T_{\text{pb}} \sim 45 \text{ ms}$, which is significantly earlier than the reference values $T_{\text{pb}} \sim 70 \text{ ms}$ in ABG15, BMG15, and also in a model of O’Connor (2014). This means that the lepton number loss from PNS is less than those previous studies since it can be measured roughly by the time integration of $L_{\nu_e}/\varepsilon_{\nu_e} - L_{\bar{\nu}_e}/\varepsilon_{\bar{\nu}_e}$. However, our 1D spherical test, albeit in the Newtonian limit, shown in Appendix B, does not exhibit such inconsistency and shows quite reasonable neutrino profiles with a previous study. We therefore consider that the reason for less agreement, especially seen in L_{ν_e} , mainly comes from the spatial advection term in the Cartesian coordinates and not from the local neutrino matter interaction terms.

We also compare the neutrino spectral difference in Figure 16. In the figure, we show time evolutions of the rms energies of emergent neutrinos $E_{\nu, \text{rms}}$ measured at the surface of cubic box with 1000 km width. For $E_{\nu, \text{rms}}$, we use the same definition as in Liebendörfer et al. (2005) and it is defined as below:

$$E_{\nu, \text{rms}} \equiv \sqrt{\frac{\int d\varepsilon f(\nu, \varepsilon) \varepsilon^4}{\int d\varepsilon f(\nu, \varepsilon) \varepsilon^2}}. \quad (74)$$

Again in Figure 16, we plot averaged value $\langle E_{\nu, \text{rms}} \rangle$ over the surface of the cubic box. From the figure, we find good agreement with the reference codes and differences are less than $\sim 1 \text{ MeV}$ for ν_e and $\bar{\nu}_e$ and $\lesssim 2 \text{ MeV}$ for ν_X after the neutronization phase ceases $T_{\text{pb}} \gtrsim 20 \text{ ms}$. In our model 1DG15, we see a spurious second peak in the $E_{\nu_X, \text{rms}}$ profile around $T_{\text{pb}} \sim 13 \text{ ms}$. However, the second peak disappears in our model 3DG15 and we thus consider that it is most likely due to our artificial treatment for the matter velocity and is insignificant.

6. SUMMARY

In this paper, we have presented our newly developed multi-D full GR neutrino radiation hydrodynamic code. The code was designed to evolve the Einstein field equation together with the GR radiation hydrodynamic equations in a self-

consistent manner while satisfying the Hamiltonian and momentum constraints. Using an M1 closure scheme, we solved spectral neutrino transport of the radiation energy and momentum in conservative way based on a truncated moment formalism. Beside the energy and momentum conservation, we paid particular attention to the lepton number conservation, especially in the neutrino trapping regime.

We explained formally that the neutrino number is transported appropriately by solving only the energy and momentum conservation equations of the neutrino radiation field, especially focusing on the neutrino trapping regime. In addition, we showed that the advection terms in energy space are essential for reproducing the neutrino trapping.

To validate our new numerical code, we first made bottom line tests such as the diffusion test, shadow casting test, and spherical propagation in free streaming regime to check the advection term in space. In addition, the important factors in CCSN simulation, gravitational redshift and Doppler shift, are tested in a curved spacetime with a sharp velocity profile. Through these standard tests, we confirmed that our code is capable of reproducing analytical results accurately and that all source terms other than the neutrino–matter interaction terms are correctly implemented.

We then performed a practical core-collapse simulation with which we could also confirm whether the above-mentioned neutrino number conservation, especially in the trapping region, is satisfied adequately. We followed the gravitational collapse, bounce, and initial postbounce phases up to $T_{\text{pb}} \sim 50 \text{ ms}$ of a $15M_{\odot}$ star to make a detailed comparison with previous studies with Boltzmann neutrino transport. Regarding neutrino opacities, we currently employed a baseline set where inelastic neutrino–electron scattering, thermal neutrino production via pair annihilation, and nucleon–nucleon bremsstrahlung were included. We started the code comparison before core bounce. Important features such as the evolution of the central Y_I and entropy as well as the neutrino trapping density showed nice agreement with the reference models. Next we made the code comparison after bounce until the stall of the bounce shock. At this transient phase, we checked that the M1 code can capture the overall evolution in the Boltzmann codes regarding the neutrino propagation from the opaque to the transparent region. Considering our insufficient resolution and the difference coordinates used, the neutrino luminosity and the energy spectrum of our code showed good agreements with the reference results. The peak luminosity ($L_{\nu_e, \text{peak}} = 3.9 \times 10^{53} \text{ erg s}^{-1}$) showed almost the same value with the reference models. After the neutronization, the neutrino luminosities showed consistent values though there is a systematic lower shift in the electron-type neutrino luminosity. The rms energies of the emergent neutrinos showed a similar level of the match with the reference results, which demonstrates the validity of our code.

In the end, we briefly discuss for the future run (using Exa-scale platforms) in order to check a numerical convergence of our 3D results and to get a closer match with the Boltzmann results in the much longer postbounce phase. As already mentioned, we were forced to adopt a low numerical resolution in this study (effective angular resolution behind the stalled shock $\sim 120 \text{ km}$ is $\sim 8 \text{ km}/120 \text{ km} \sim 3^{\circ}.8$) due to our limited computational resource. The code has already been tuned to get a high parallel efficiency ($\gtrsim 90\%$, e.g., going from 2048 to 4096

cores) with a very high performance efficiency ($\sim 32\%$) which measures the ratio of the real performance of our code to the theoretical peak performance measured by the platform, Cray XC30 in our case. However, it still takes ~ 1.25 CPU days to follow ~ 1 ms postbounce in model 3DG15 by the peta-flops machine occupying $\sim 10\%$ of its total resource (2048 processors). By only comparing the angular resolution $\lesssim 2^\circ$ of recent numerical studies (e.g., Hanke et al. 2013; Müller & Janka 2014; Takiwaki et al. 2014), the employed resolution in this study is approximately two times coarser. Currently, the wall clock time per each time step in the postbounce phase (the typical numerical time step $\Delta t = 10^{-7}$ s) is ~ 5 s if we use 4096 processors (i.e., we can follow the postbounce time of ~ 1.7 ms per day, which we write as 1.7 ms day^{-1} in the following). With this performance, we estimate how much computational resources and how much computational time are required for the twice high-resolution model to follow ~ 200 ms after bounce, e.g., until the shock revival is expected to occur for low-mass progenitor stars in 3D (e.g., Takiwaki et al. 2014; Melson et al. 2015). Since our current resolution at the origin $\Delta x \sim 480$ m is marginally acceptable, we may just need to double the number of the numerical meshes in each nested box.

If we are able to double the resolution with the fixed innermost mesh size and use $4096 \times 2^3 \sim 32,000$ processors, we can also follow the same postbounce evolution $\sim 1.7 \text{ ms day}^{-1}$ or $\sim 3.4 \text{ ms day}^{-1}$ occupying $4096 \times 2^3 \times 2 \sim 64,000$ processors. Even if we can luckily take the latter case ($\sim 3.4 \text{ ms day}^{-1}$), we still need approximately two months to follow ~ 200 ms after bounce occupying the $\sim 64,000$ processors. For more massive progenitors, the shock revival in 3D models would be much more delayed than in 2D ($T_{\text{pb}} \gtrsim 600$ ms, e.g., Marek et al. 2006; Müller et al. 2012a, 2012b; Nakamura et al. 2014b). This is apparently beyond the maximum computational time allocated for the K computer and surely needs Exa-scale platforms (in the next decade to come).

Before the advent of these next-generation supercomputers, it is noted that we actually have many tasks to improve our code. We expect that we can still enhance the numerical efficiency, especially when we get a convergent solution during the Newton–Raphson iteration in the implicit update. At present, the convergence becomes worse where the energy fluxes of neutrinos F^μ/H^μ become non-negligible (i.e., just above the neutrino sphere). We have confirmed that the neutrino–electron scattering is one of the dominant factors that delays the convergence. With an eye toward the actual application of this code in CCSN simulations, we plan to continue our code refinement, in which we not only need to employ a more elaborate set of neutrino opacities (e.g., Horowitz 2002; Burrows et al. 2006; Sumiyoshi & Röpke 2008; Martínez-Pinedo et al. 2012; Fischer et al. 2013; Bartl et al. 2014) with including the higher order angular dependence of the reaction angle that was omitted for simplicity (e.g., Section 5.1), but also to find a more efficient algorithm to deal with the resulting (more complicated) Jacobi matrix in the implicit update. This study is only our very first step toward a more realistic coding, which is indispensable for quantitative study of stellar core-collapse and the explosion mechanism.

This work was supported by the European Research Council (ERC; FP7) under the ERC Advanced grant Agreement No. 321263—FISH. T.K. acknowledges fruitful discussions with

M. Liebendörfer, R.M. Cabezón, M. Hempel, and K.-C. Pan. We acknowledge A. Imakura for his useful advice for an efficient matrix inversion scheme. T.T. and K.K. are grateful to K. Sato and S. Yamada for continuing encouragements. Numerical computations were carried out on the Cray XC30 at the Center for Computational Astrophysics, National Astronomical Observatory of Japan. This study was supported by the Ministry of Education, Science, and Culture of Japan (Nos. 24103006, 24244036, 26707013, and 26870823) and by the HPCI Strategic Program of Japanese MEXT.

APPENDIX A NEUTRINO MATTER INTERACTION TERMS

In this appendix, we summarize the neutrino matter interaction processes included in this study, which are as follow: absorption and emission processes

$$\nu_e n \leftrightarrow e^- p, \quad (75)$$

$$\bar{\nu}_e p \leftrightarrow e^+ n, \quad (76)$$

$$\nu_e A \leftrightarrow e^- A'; \quad (77)$$

isoenergy scattering of neutrinos off nucleons and heavy nuclei

$$\nu n \leftrightarrow \nu n, \quad (78)$$

$$\nu p \leftrightarrow \nu p, \quad (79)$$

$$\nu A \leftrightarrow \nu A; \quad (80)$$

inelastic neutrino electron scattering

$$\nu e \leftrightarrow \nu e; \quad (81)$$

thermal neutrino pair production and annihilation

$$e^- e^+ \leftrightarrow \nu \bar{\nu}; \quad (82)$$

and nucleon–nucleon bremsstrahlung

$$NN \leftrightarrow NN\nu\bar{\nu}. \quad (83)$$

The four vector neutrino matter interaction term S^μ is given by summation of all these interaction terms as

$$S^\mu \equiv S^{\text{nae},\mu} + S^{\text{iso},\mu} + S^{\text{nes},\mu} + S^{\text{tp},\mu} + S^{\text{brem},\mu}, \quad (84)$$

where $S^{\text{nae},\mu}$, $S^{\text{iso},\mu}$, $S^{\text{nes},\mu}$, $S^{\text{tp},\mu}$, and $S^{\text{brem},\mu}$ are the four vector source terms of neutrino absorption and emission (nae), isoenergy scattering of neutrinos off nucleons and heavy nuclei (iso), inelastic neutrino electron scattering (nes), thermal neutrino pair production and annihilation (tp), and nucleon–nucleon Bremsstrahlung (brem), respectively.

We briefly summarize each interacting kernels, opacities, and source terms in the following subsections. For more detailed expressions and explanations, the reader is referred to Bruenn (1985), Hannestad & Raffelt (1998), and Rampp & Janka (2002). The derivation of the four vector source term from these quantities is given by Shibata et al. (2011).

A.1. Neutrino Absorption and Emission

We consider that neutrino absorption and emission: by free neutrons $\nu_e n \leftrightarrow e^- p$, by free protons $\bar{\nu}_e p \leftrightarrow e^+ n$, and by heavy nuclei $\nu_e A \leftrightarrow e^- A'$. The four vector source term

$S^{\text{nae},\mu}$ is given by

$$S_{(\nu,\varepsilon)}^{\text{nae},\mu} = \kappa_{(\nu,\varepsilon)}^{\text{nae}} \left[\left(\frac{4\pi\varepsilon^3}{\exp\{\beta(\varepsilon - \mu_\nu)\} + 1} - J_{(\nu,\varepsilon)} \right) \mu^\mu - H_{(\nu,\varepsilon)}^\mu \right], \quad (85)$$

where κ^{nae} is the opacity, $\beta = 1/k_B T$ with k_B the Boltzmann's constant, and $\mu_{\bar{\nu}_e} = -\mu_{\bar{\nu}_e} = \mu_e - \mu_p + \mu_n$ is the chemical potential of neutrinos in thermal equilibrium with matter. Here, μ_e, μ_n , and μ_p are the chemical potentials of electrons, neutrons, and protons, including the rest mass energy of each particle, respectively. For each reaction ($\nu_e n \leftrightarrow e^- p$, $\bar{\nu}_e p \leftrightarrow e^+ n$ and $\nu_e A \leftrightarrow e^- A'$), we first evaluate absorptivity $1/\lambda [s^{-1}]$ and then emissivity $j [s^{-1}]$.

Absorptivity for reaction $\nu_e n \leftrightarrow e^- p$ is expressed as (Bruenn 1985; Rampp & Janka 2002)

$$\frac{1}{\lambda_\varepsilon} = \frac{c}{(\hbar c)^4} \frac{G_F^2}{\pi} (g_V^2 + 3g_A^2) \eta_{np} [1 - F_{e^-}(\varepsilon + Q)] \times (\varepsilon + Q) \sqrt{(\varepsilon + Q)^2 - m_e^2 c^4}, \quad (86)$$

where we employed $g_V = 1$ and $g_A = 1.23$ as form factors resulting from the virtual strong interaction processes. $F_x(\varepsilon) \equiv [1 + \exp(\beta(\varepsilon - \mu_x))]^{-1}$ is the Fermi distribution function of fermion x with energy ε . $G_F (= 8.957 \times 10^{-44} \text{ MeV cm}^3)$ is the Fermi constant.

For the reaction $\bar{\nu}_e p \leftrightarrow e^+ n$,

$$\frac{1}{\lambda_\varepsilon} = \begin{cases} \frac{c}{(\hbar c)^4} \frac{G_F^2}{\pi} (g_V^2 + 3g_A^2) \eta_{pn} [1 - F_{e^+}(\varepsilon - Q)] \\ \quad (\varepsilon - Q) \sqrt{(\varepsilon - Q)^2 - m_e^2 c^4}, \\ \quad \text{for } \varepsilon \geq m_e c^2 + Q \\ 0, \\ \text{otherwise,} \end{cases} \quad (87)$$

where $Q = m_n c^2 - m_p c^2$ is the rest mass energy difference of the neutron and proton.

Finally, for the reaction $\nu_e A \leftrightarrow e^- A'$,

$$\frac{1}{\lambda_\varepsilon} = \begin{cases} e^{-\beta\Delta} \frac{c}{(\hbar c)^4} \frac{G_F^2}{\pi} g_A^2 \frac{2}{7} N_p N_h n_A [1 - F_{e^-}(\varepsilon + Q')] \\ \quad (\varepsilon + Q') \sqrt{(\varepsilon + Q')^2 - m_e^2 c^4}, \\ \quad \text{for } \varepsilon \geq m_e c^2 - Q' \\ 0, \\ \text{otherwise,} \end{cases} \quad (88)$$

where $Q' \equiv \mu_n - \mu_p + \Delta$ is the mass difference between the initial and the final states through the reaction. By following Bruenn (1985) and Rampp & Janka (2002), we employed

$\Delta = 3 \text{ MeV}$ and

$$N_p = \begin{cases} 0, & \text{for } Z < 20 \\ Z - 20, & \text{for } 20 < Z < 28 \\ 8, & \text{for } Z > 28, \end{cases} \quad (89)$$

$$N_h = \begin{cases} 6, & \text{for } N < 34 \\ 40 - N, & \text{for } 34 < N < 40 \\ 0, & \text{for } N > 40, \end{cases} \quad (90)$$

for the number of protons N_p and holes N_h in the dominant GT resonance for the electron capture.

As for the values η_{pn} and η_{np} , we adopted those proposed in Bruenn (1985) and Rampp & Janka (2002),

$$\eta_{pn} = \frac{n_n - n_p}{\exp(\beta(\mu_n - \mu_p - Q)) - 1}, \quad (91)$$

$$\eta_{np} = \frac{n_p - n_n}{\exp(-\beta(\mu_n - \mu_p - Q)) - 1}, \quad (92)$$

while we set

$$\eta_{pn} = n_p, \quad (93)$$

$$\eta_{np} = n_n, \quad (94)$$

in the non-degeneracy regime where $\mu_n - \mu_p - Q < 0.01 \text{ MeV}$ is met.

Once we evaluate the absorptivity, the emissivity j and the opacity κ are obtained as (Bruenn 1985)

$$j_\varepsilon = e^{\beta(\varepsilon - \mu_\nu)} \frac{1}{\lambda_\varepsilon}, \quad (95)$$

and

$$\kappa_{(\varepsilon)}^{\text{nae}} = j_\varepsilon + \frac{1}{\lambda_\varepsilon}. \quad (96)$$

A.2. Isoenergy Scattering of Neutrinos

The four vector source term for isoenergetic scattering of neutrinos off free nucleons and heavy nuclei is written as (Shibata et al. 2011)

$$S_{(\varepsilon)}^{\text{iso},\mu} = -\chi_{(\varepsilon)}^{\text{iso}} H_{(\varepsilon)}^\mu. \quad (97)$$

To evaluate $\chi_{(\varepsilon)}^{\text{iso}}$ from the isoenergetic scattering kernel $R^{\text{iso}}(\varepsilon, \omega)$, we expand it into a Legendre series in terms of ω (here ω is the cosine of the scattering angle) up to the first order as

$$R^{\text{iso}}(\varepsilon, \omega) \approx \frac{1}{2} \Phi_{(\varepsilon)}^{\text{iso},0} + \frac{3}{2} \omega \Phi_{(\varepsilon)}^{\text{iso},1}, \quad (98)$$

where $\Phi_{(\varepsilon)}^{\text{iso},0}$ and $\Phi_{(\varepsilon)}^{\text{iso},1}$ are the zeroth and first order of scattering kernels, respectively. After angular integration of the angular-dependent source term with respect to ω , $\chi_{(\varepsilon)}^{\text{iso}}$ is expressed as below (Shibata et al. 2011):

$$\chi_{(\varepsilon)}^{\text{iso}} = \varepsilon^2 (\Phi_{(\varepsilon)}^{\text{iso},0} - \Phi_{(\varepsilon)}^{\text{iso},1}). \quad (99)$$

For the scattering process on the free nucleon (n/p), the zeroth- and first-order kernels become

$$\Phi_{(\varepsilon)}^{\text{iso},0} = \frac{2\pi}{(hc)^3} \frac{G_F^2}{2\pi h} \eta_{NN} ((h\nu^N)^2 + 3(h_A^N)^2), \quad (100)$$

$$\Phi_{(\varepsilon)}^{\text{iso},1} = \frac{2\pi}{(hc)^3} \frac{G_F^2}{2\pi h} \eta_{NN} ((h_V^N)^2 - (h_A^N)^2). \quad (101)$$

Obviously, $\Phi_{(\varepsilon)}^{\text{iso},0/1}$ has a dimension $\text{MeV}^{-2} \text{s}^{-1}$ and $\chi_{(\varepsilon)}^{\text{iso}}$ thus has a dimension s^{-1} . In the above, N takes n (neutron) or p (proton) and h_V^N and h_A^N are defined as (Bruenn 1985)

$$h_V^n = -\frac{1}{2}, \quad (102)$$

$$h_V^p = \frac{1}{2} - 2\sin^2 \theta_W, \quad (103)$$

$$h_A^n = -\frac{1}{2}g_A, \quad (104)$$

$$h_A^p = \frac{1}{2}g_A, \quad (105)$$

where θ_W is the Weinberg angle and we adopt the value $\sin^2 \theta_W = 0.2325$. By following Mezzacappa & Bruenn (1993c) and Rapp & Janka (2002), we evaluate η_{NN} as

$$\eta_{NN} = n_N \frac{\xi_N}{\sqrt{1 + \xi_N^2}}, \quad (106)$$

$$\xi_N = \frac{3}{2\beta E_N^F}, \quad (107)$$

$$E_N^F = \frac{(\hbar c)^2}{2m_N c^2} (3\pi^2 n_N)^{2/3}. \quad (108)$$

Next, for coherent scattering on heavy nuclei, the zeroth- and first-order kernels become (Bruenn 1985)

$$\begin{aligned} \Phi_{(\varepsilon)}^{\text{iso},0} &= \frac{2\pi}{(hc)^3} \frac{G_F^2}{4\pi h} n_A \left(AC_V^0 - \left(\frac{1}{2}A - Z \right) C_V^1 \right)^2 \\ &\quad \times \left(\frac{2y - 1 + e^{-2y}}{y^2} \right), \end{aligned} \quad (109)$$

$$\begin{aligned} \Phi_{(\varepsilon)}^{\text{iso},1} &= \frac{2\pi}{(hc)^3} \frac{G_F^2}{4\pi h} n_A \left(AC_V^0 - \left(\frac{1}{2}A - Z \right) C_V^1 \right)^2 \\ &\quad \times \left(\frac{2 - 3y + 2y^2 - (2 + y)e^{-2y}}{y^3} \right), \end{aligned} \quad (110)$$

with $C_{V/A}^0 = (h_{V/A}^p + h_{V/A}^n)/2$, $C_{V/A}^1 = (h_{V/A}^p - h_{V/A}^n)$, $y = 4b\varepsilon^2$, and $b = 4.8 \times 10^{-6} A^{2/3}$. Here n_A , A , and Z denote the number density of heavy nuclei, the atomic number, and the charge, respectively.

A.3. Neutrino Electron Scattering

Inelastic scattering of neutrinos off electrons plays important role to help neutrinos escape more freely from the center as a consequence of down-scattering and it thus enhances deleptonization of central core. The source term $S_{(\varepsilon)}^{\text{nes},\mu}$ is expressed in terms of the collision integral $B_{(\varepsilon,\Omega)}^{\text{nes}}$ as (Shibata et al. 2011)

$$S_{(\varepsilon)}^{\text{nes},\mu} = \varepsilon^3 \int d\Omega B_{(\varepsilon,\Omega)}^{\text{nes}} (u^\mu + l^\mu), \quad (111)$$

where l^μ is a unit normal four vector orthogonal to u^μ . The collision integral $B_{(\varepsilon,\Omega)}^{\text{nes}}$ along the propagation direction Ω is

expressed as

$$\begin{aligned} B_{(\varepsilon,\Omega)}^{\text{nes}} &= \int \varepsilon'^2 d\varepsilon' d\Omega' [f(\varepsilon', \Omega') \{1 - f(\varepsilon, \Omega)\} R^{\text{nes},\text{in}}(\varepsilon, \varepsilon', \omega) \\ &\quad - \{1 - f(\varepsilon', \Omega')\} f(\varepsilon, \Omega) R^{\text{nes},\text{out}}(\varepsilon, \varepsilon', \omega)], \end{aligned} \quad (112)$$

where $R^{\text{nes},\text{in}/\text{out}}(\varepsilon, \varepsilon', \omega)$ is the angular-dependent inward/outward scattering kernel and ω is the cosine of scattering angle, i.e., angle between Ω and Ω' . With expanding the angular-dependent inward/outward scattering kernel $R^{\text{nes},\text{in}/\text{out}}(\varepsilon, \varepsilon', \omega)$ into a Legendre series with respect to ω and taking up to the first order as

$$R^{\text{nes},\text{in}/\text{out}}(\varepsilon, \varepsilon', \omega) \approx \frac{1}{2} \Phi_{(\varepsilon,\varepsilon')}^{\text{nes},\text{in}/\text{out},0} + \frac{3}{2} \omega \Phi_{(\varepsilon,\varepsilon')}^{\text{nes},\text{in}/\text{out},1}, \quad (113)$$

and with decomposing the neutrino distribution function after scattering into isotropic and non-isotropic parts as

$$f(\varepsilon', \Omega') \approx f^0(\varepsilon') + f^{1,\mu}(\varepsilon') l'_\mu, \quad (114)$$

the final expression of the scattering integral is described as

$$B_{(\varepsilon,\Omega)}^{\text{nes}} = f(\varepsilon, \Omega) (A_{(\varepsilon),\text{nes}}^0 + B_{(\varepsilon),\text{nes}}^{0,\mu} l_\mu) + C_{(\varepsilon),\text{nes}}^0 + C_{(\varepsilon),\text{nes}}^{1,\mu} l_\mu. \quad (115)$$

In the above, we used the same notations used in Bruenn (1985; see their Equations (108)–(113)) for $A_{(\varepsilon),\text{nes}}^0$, $B_{(\varepsilon),\text{nes}}^{0,\mu}$, $C_{(\varepsilon),\text{nes}}^0$, and $C_{(\varepsilon),\text{nes}}^{1,\mu}$ with the exception of $B_{(\varepsilon),\text{nes}}^{0,\mu}$ and $C_{(\varepsilon),\text{nes}}^{1,\mu}$ which have three spatial components (the zeroth component is determined from orthogonality $H^\mu u_\mu = 0$) and of $B_{(\varepsilon),\text{nes}}^{0,\mu}$, which is a factor of 3 larger than that of Equation (109) in Bruenn (1985). They are explicitly written as

$$\begin{aligned} A_{(\varepsilon),\text{nes}}^0 &= -\frac{2\pi}{(hc)^3} \int \varepsilon'^2 d\varepsilon' [f^0(\varepsilon') \Phi_{(\varepsilon,\varepsilon')}^{\text{nes},\text{in},0} \\ &\quad + (1 - f^0(\varepsilon')) \Phi_{(\varepsilon,\varepsilon')}^{\text{nes},\text{out},0}], \end{aligned} \quad (116)$$

$$B_{(\varepsilon),\text{nes}}^{0,\mu} = -\frac{2\pi}{(hc)^3} \int \varepsilon'^2 d\varepsilon' f^{1,\mu}(\varepsilon') (\Phi_{(\varepsilon,\varepsilon')}^{\text{nes},\text{in},1} - \Phi_{(\varepsilon,\varepsilon')}^{\text{nes},\text{out},1}), \quad (117)$$

$$C_{(\varepsilon),\text{nes}}^0 = \frac{2\pi}{(hc)^3} \int \varepsilon'^2 d\varepsilon' f^0(\varepsilon') \Phi_{(\varepsilon,\varepsilon')}^{\text{nes},\text{in},0}, \quad (118)$$

$$C_{(\varepsilon),\text{nes}}^{1,\mu} = \frac{2\pi}{(hc)^3} \int \varepsilon'^2 d\varepsilon' f^{1,\mu}(\varepsilon') \Phi_{(\varepsilon,\varepsilon')}^{\text{nes},\text{in},1}, \quad (119)$$

where we employ

$$f^0(\varepsilon) = \frac{J(\varepsilon)}{4\pi\varepsilon^3}, \quad (120)$$

$$f^{1,\mu}(\varepsilon) = \frac{3H_{(\varepsilon)}^\mu}{4\pi\varepsilon^3}, \quad (121)$$

for the isotropic and non-isotropic parts of the distribution function (see also Shibata et al. 2011). For an explicit evaluation for $\Phi_{(\varepsilon,\varepsilon')}^{\text{nes},\text{in}/\text{out},0/1}$, we refer the reader to Yueh & Buchler (1976) and Bruenn (1985).

Since coefficients (116)–(119) do not depend on the propagation direction Ω , the final integral Equation (111) with

imposing Equation (115) becomes

$$\begin{aligned} S_{(\varepsilon)}^{\text{nes},\mu} &= (J_{(\varepsilon)} u^\mu + H_{(\varepsilon)}^\mu) A_{(\varepsilon),\text{nes}}^0 \\ &+ (H_{\alpha(\varepsilon)} u^\mu + L_{\alpha(\varepsilon)}^\mu) B_{(\varepsilon),\text{nes}}^{0,\alpha} \\ &+ 4\pi\varepsilon^3 u^\mu C_{(\varepsilon),\text{nes}}^0 \\ &+ \frac{4\pi\varepsilon^3}{3} h_{\alpha\mu} C_{(\varepsilon),\text{nes}}^{1,\alpha}, \end{aligned} \quad (122)$$

where $h_{\mu\nu} \equiv g_{\mu\nu} + u_\mu u_\nu$ is the projection operator. Since Φ^{nes} has a unit [$\text{cm}^3 \text{s}^{-1}$], $A_{(\varepsilon),\text{nes}}^0$, $B_{(\varepsilon),\text{nes}}^{0,\mu}$, $C_{(\varepsilon),\text{nes}}^0$, and $C_{(\varepsilon),\text{nes}}^{1,\mu}$ thus have a unit [s^{-1}] which is required to let the dimension of $S_{(\varepsilon)}^{\text{nes},\mu}$ to be [$\text{MeV}^3 \text{s}^{-1}$].

A.4. Thermal Pair Production and Annihilation of Neutrinos

As for the thermal pair production/annihilation process of neutrinos, we take the same approach as the neutrino electron scattering process. The collision integral $B_{(\varepsilon,\Omega)}^{\text{tp}}$ is expressed as

$$\begin{aligned} B_{(\varepsilon,\Omega)}^{\text{nes}} &= \int \varepsilon'^2 d\varepsilon' d\Omega' [\{1 - \bar{f}(\varepsilon', \Omega')\} \\ &\times \{1 - f(\varepsilon, \Omega)\} R^{\text{tp,pro}}(\varepsilon, \varepsilon', \omega) \\ &- \bar{f}(\varepsilon', \Omega') f(\varepsilon, \Omega) R^{\text{tp,ann}}(\varepsilon, \varepsilon', \omega)], \end{aligned} \quad (123)$$

where \bar{f} denotes the anti-neutrino distribution function and $R^{\text{tp,pro/ann}}(\varepsilon, \varepsilon', \omega)$ is the angular-dependent production/annihilation kernel. We again expand the kernel $R^{\text{tp,pro/ann}}(\varepsilon, \varepsilon', \omega)$ up to the first order in ω as

$$R^{\text{tp,pro/ann}}(\varepsilon, \varepsilon', \omega) \approx \frac{1}{2} \Phi_{(\varepsilon,\varepsilon')}^{\text{tp,pro/ann},0} + \frac{3}{2} \omega \Phi_{(\varepsilon,\varepsilon')}^{\text{tp,pro/ann},1}, \quad (124)$$

and the final expression of the scattering integral is thus described as

$$B_{(\varepsilon,\Omega)}^{\text{tp}} = f(\varepsilon, \Omega) (A_{(\varepsilon),\text{tp}}^0 + B_{(\varepsilon),\text{tp}}^{0,\mu} l_\mu) + C_{(\varepsilon),\text{tp}}^0 + C_{(\varepsilon),\text{tp}}^{1,\mu} l_\mu, \quad (125)$$

which has exactly the same expression as that of the neutrino electron scattering (Equation (115)). Again, coefficients have the same notations as in Bruenn (1985; see their Equations (117)–(121)) and described as

$$\begin{aligned} A_{(\varepsilon),\text{tp}}^0 &= -\frac{2\pi}{(hc)^3} \int \varepsilon'^2 d\varepsilon' [\{1 - \bar{f}^0(\varepsilon')\} \Phi_{(\varepsilon,\varepsilon')}^{\text{tp,pro},0} \\ &+ \bar{f}^0(\varepsilon') \Phi_{(\varepsilon,\varepsilon')}^{\text{tp,ann},0}], \end{aligned} \quad (126)$$

$$B_{(\varepsilon),\text{tp}}^{0,\mu} = \frac{2\pi}{(hc)^3} \int \varepsilon'^2 d\varepsilon' \bar{f}^{1,\mu}(\varepsilon') (\Phi_{(\varepsilon,\varepsilon')}^{\text{tp,pro},1} - \Phi_{(\varepsilon,\varepsilon')}^{\text{tp,ann},1}), \quad (127)$$

$$C_{(\varepsilon),\text{tp}}^0 = \frac{2\pi}{(hc)^3} \int \varepsilon'^2 d\varepsilon' \{1 - \bar{f}^0(\varepsilon')\} \Phi_{(\varepsilon,\varepsilon')}^{\text{tp,pro},0}, \quad (128)$$

$$C_{(\varepsilon),\text{tp}}^{1,\mu} = -\frac{2\pi}{(hc)^3} \int \varepsilon'^2 d\varepsilon' \bar{f}^{1,\mu}(\varepsilon') \Phi_{(\varepsilon,\varepsilon')}^{\text{tp,pro},1}. \quad (129)$$

For an explicit evaluation for $\Phi_{(\varepsilon,\varepsilon')}^{\text{tp,pro/ann},0/1}$, we refer the reader to Bruenn (1985). The final expression of the source term $S_{(\varepsilon)}^{\text{tp},\mu}$ is simply obtained by replacing coefficients in Equation (122) with those of thermal process, i.e., with Equations (126)–(129).

A.5. Nucleon–Nucleon Bremsstrahlung

The collision integral for Nucleon-nucleon Bremsstrahlung $B_{(\varepsilon,\Omega)}^{\text{br}}$ has the same expression as that of the thermal pair production/annihilation of neutrinos and therefore the same notations used in Appendix A.4 can be directly applicable. $B_{(\varepsilon,\Omega)}^{\text{br}}$ is written as

$$\begin{aligned} B_{(\varepsilon,\Omega)}^{\text{br}} &= \int \varepsilon'^2 d\varepsilon' d\Omega' [\{1 - \bar{f}(\varepsilon', \Omega')\} \\ &\times \{1 - f(\varepsilon, \Omega)\} R^{\text{br,pro}}(\varepsilon, \varepsilon', \omega) \\ &- \bar{f}(\varepsilon', \Omega') f(\varepsilon, \Omega) R^{\text{br,ann}}(\varepsilon, \varepsilon', \omega)], \end{aligned} \quad (130)$$

where $R^{\text{br,pro/ann}}(\varepsilon, \varepsilon', \omega)$ is the production/annihilation kernel. As for the Bremsstrahlung process, we again expand the kernel $R^{\text{br,pro/ann}}(\varepsilon, \varepsilon', \omega)$ into a Legendre series, but take only the zeroth order term in ω for simplicity. Then the kernel becomes

$$R^{\text{br,pro/ann}}(\varepsilon, \varepsilon', \omega) \approx \frac{1}{2} \Phi_{(\varepsilon,\varepsilon')}^{\text{br,pro/ann},0}. \quad (131)$$

Coefficients used in the final expression for the collision integral and the source term are simply evaluated by replacing Φ^{tp} in Equations (126)–(129) with Φ^{br} .

Isotropic production kernel $\Phi_{(\varepsilon,\varepsilon')}^{\text{br,pro},0}$ can be evaluated by following manner.

$$\Phi_{(\varepsilon,\varepsilon')}^{\text{br,pro},0} \equiv e^{-\beta(\varepsilon+\varepsilon')} \sum_{i \in \text{nn,pp,np}} \min(\phi_{\text{br}}^{\text{D},i}(\varepsilon, \varepsilon'), \phi_{\text{br}}^{\text{ND},i}(\varepsilon, \varepsilon')). \quad (132)$$

In the above equation, indexes D and ND denote the degenerate and non-degenerate limit of free nucleons, respectively, and (nn, pp, np) represent bremsstrahlung due to neutron–neutron, proton–proton, and neutron–proton pair, respectively. $\phi_{\text{br}}^{\text{D},i}(\varepsilon, \varepsilon')$ and $\phi_{\text{br}}^{\text{ND},i}(\varepsilon, \varepsilon')$ are expressed as

$$\begin{aligned} \phi_{\text{br}}^{\text{D},i}(\varepsilon, \varepsilon') &= (\hbar c)^6 \frac{G^2}{4} \left(\frac{2\pi f}{m_\pi} \right)^4 \\ &\times \frac{m_i^4}{12\pi^9} \frac{1}{\beta^2(\varepsilon + \varepsilon')} \frac{(4\pi^2 + \beta^2(\varepsilon + \varepsilon')^2) \alpha_i}{1 - e^{-\beta(\varepsilon + \varepsilon')}} \frac{1}{S_i} \\ &\times \left[\frac{2\hbar c (3\pi^2 X_i n_b)^{\frac{1}{3}}}{(\hbar c)^6} \right], \end{aligned} \quad (133)$$

$$\begin{aligned} \phi_{\text{br}}^{\text{ND},i}(\varepsilon, \varepsilon') &= (\hbar c)^6 \frac{G^2}{4} \left(\frac{2\pi f}{m_\pi} \right)^4 \\ &\times \frac{2m_i^{3/2}}{\pi^{11/2}} \frac{1}{\beta^{1/2}(\varepsilon + \varepsilon')^2} \sqrt{1 + \beta(\varepsilon + \varepsilon')} \\ &\times \frac{\alpha_i X_i^2 n_b^2}{S_i}. \end{aligned} \quad (134)$$

In the above equations, $\phi_{\text{br}}^{\text{D/ND},i}(\varepsilon, \varepsilon')$ have a dimension in [$\text{cm}^3 \text{s}^{-1}$], $f = 1$ and $G^2 = c(\hbar c)^2 G_F^2 = 1.55 \times 10^{-33}$

[MeV⁻² cm³ s⁻¹]. We employed values for α_i , X_i , m_i , and S_i as

$$\alpha_i = \begin{pmatrix} 3g_A^2 \\ 3g_A^2 \\ \frac{7}{2}g_A^2 \end{pmatrix}, \quad X_i = \begin{pmatrix} X_n \\ X_p \\ \min(X_n, X_p) \end{pmatrix}, \quad m_i = \begin{pmatrix} m_n \\ m_p \\ \sqrt{m_n m_p} \end{pmatrix},$$

$$S_i = \begin{pmatrix} 4 \\ 4 \\ 1 \end{pmatrix}, \quad \text{for } i = \begin{pmatrix} nn \\ pp \\ np \end{pmatrix}. \quad (135)$$

After deriving the production kernel, we can obtain the annihilation one by using a following relation

$$R^{\text{br,ann}}(\varepsilon, \varepsilon', \omega) = e^{\beta(\varepsilon+\varepsilon')} R^{\text{br,pro}}(\varepsilon, \varepsilon', \omega). \quad (136)$$

A.6. Summary of the Source Term and Mean Free Paths

By combining all the source terms mentioned above, the final expression becomes

$$S_{(\varepsilon)}^\mu = \kappa_{(\varepsilon)}^{\text{nae}} \{ (J_{(\varepsilon)}^{\text{eq}} - J_{(\varepsilon)}) u^\mu - H_{(\varepsilon)}^\mu \} - \chi_{(\varepsilon)}^{\text{iso}} H_{(\varepsilon)}^\mu$$

$$+ \sum_{X \in \text{nes, tp, br}} \{ (J_{(\varepsilon)} u^\mu + H_{(\varepsilon)}^\mu) A_{(\varepsilon), X}^0 + 4\pi\varepsilon^3 u^\mu C_{(\varepsilon), X}^0 \}$$

$$+ \{ (H_{\alpha(\varepsilon)} u^\mu + L_{\alpha(\varepsilon)}^\mu) B_{(\varepsilon), X}^{0, \alpha} + \frac{4\pi\varepsilon^3}{3} h_{\alpha}^\mu C_{(\varepsilon), X}^{1, \alpha} \}, \quad (137)$$

where $J_{(\varepsilon)}^{\text{eq}}$ is written by

$$J_{(\varepsilon)}^{\text{eq}} = \frac{4\pi\varepsilon^3}{\exp\{\beta(\varepsilon - \mu_\nu)\} + 1}. \quad (138)$$

In the end, we plot inverse mean free paths of each process for reference. Assumed hydrodynamical profiles are $\rho = 10^{10}$ g cm⁻³, $T = 0.638$ MeV, and $Y_e = 0.43$ (Figure 17), which corresponds to the central profile of “s15s7b2” in Woosley & Weaver (1995), $\rho = 10^{11}$ g cm⁻³, $T = 1.382$ MeV, and $Y_e = 0.4$ (Figure 18), which is the same condition used in Figure 36 in Bruenn (1985), and $\rho = 10^{13}$ g cm⁻³, $T = 3$ MeV, and $Y_e = 0.25$ (Figure 19), which is a typical profile after neutrino trapping during collapse phase. As in Bruenn (1985), we assumed the final state occupancy of the neutrinos is zero. More explicitly, we plot $1/\lambda_{\text{mfp}}$ [cm⁻¹] expressed by

$$\lambda_{\text{mfp}}^{-1} = \frac{1}{c} \begin{cases} \kappa_{(\nu, \varepsilon)}^{\text{nae}}, & \text{(neutrino absorption and emission)} \\ \chi_{(\varepsilon)}^{\text{iso}}, & \text{(isoenergy scattering)} \\ A_{(\varepsilon), \text{nes}}^0, & \text{(neutrino electron scattering)} \\ A_{(\varepsilon), \text{tp}}^0, & \text{(thermal pair production and annihilation)} \\ A_{(\varepsilon), \text{br}}^0, & \text{(nucleon–nucleon bremsstrahlung).} \end{cases} \quad (139)$$

Since the isoenergy scattering rate has the same value for all neutrino species, we only plotted for electron-type neutrinos. Note that the inverse mean free path for bremsstrahlung is multiplied by 10¹⁵ (Figure 17), 10¹⁰ (Figure 18), and 10⁵ (Figure 19), and for the thermal process it is multiplied by 10¹⁰ (Figures 17–19).

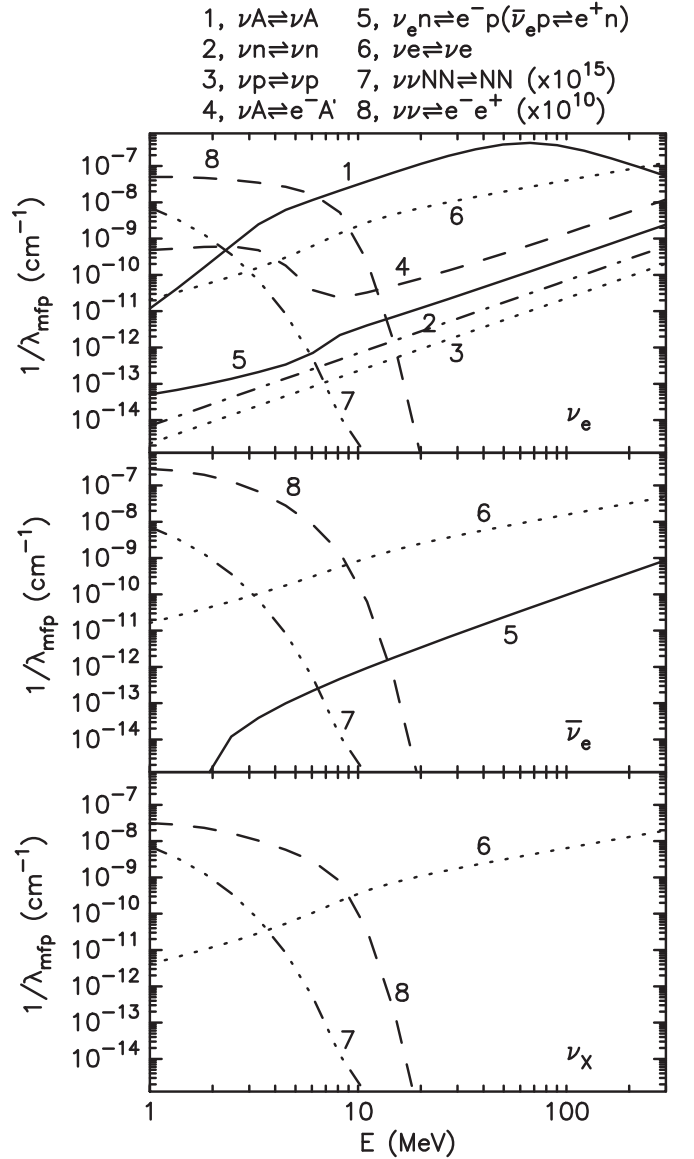


Figure 17. Energy dependence of the inverse mean free paths for each process labeled at the top part. The hydrodynamical background employed is $\rho = 10^{10}$ g cm⁻³, $T = 0.638$ MeV, and $Y_e = 0.43$ and we assumed the final state occupancy of the neutrinos is zero. With using the EOS of Lattimer & Douglas Swesty (1991) with compressibility parameter $K = 220$ MeV, several representative thermodynamical quantities become $s = 0.71 k_B$ baryon⁻¹, $A = 65.5$, and $Z = 28.2$.

APPENDIX B COMPARISON IN 1D SPHERICAL COORDINATE

In this appendix, we perform a core-collapse simulation using 1D spherical symmetric M1 neutrino transport code. The aim of this section is to test the local neutrino–matter interaction terms implemented in our main 3D Cartesian grid-based radiation-hydrodynamics code. Since our 3D multi-energy neutrino radiation-hydrodynamics code with higher resolution than the one used in Section 5 is still computationally demanding, it is not easy to check the spatial resolution dependence on the practical core-collapse simulation. Therefore, we cannot assess whether the differences between our (pseudo-)1D results and previous 1D ones come from the spatial advection terms or from the neutrino–matter interaction

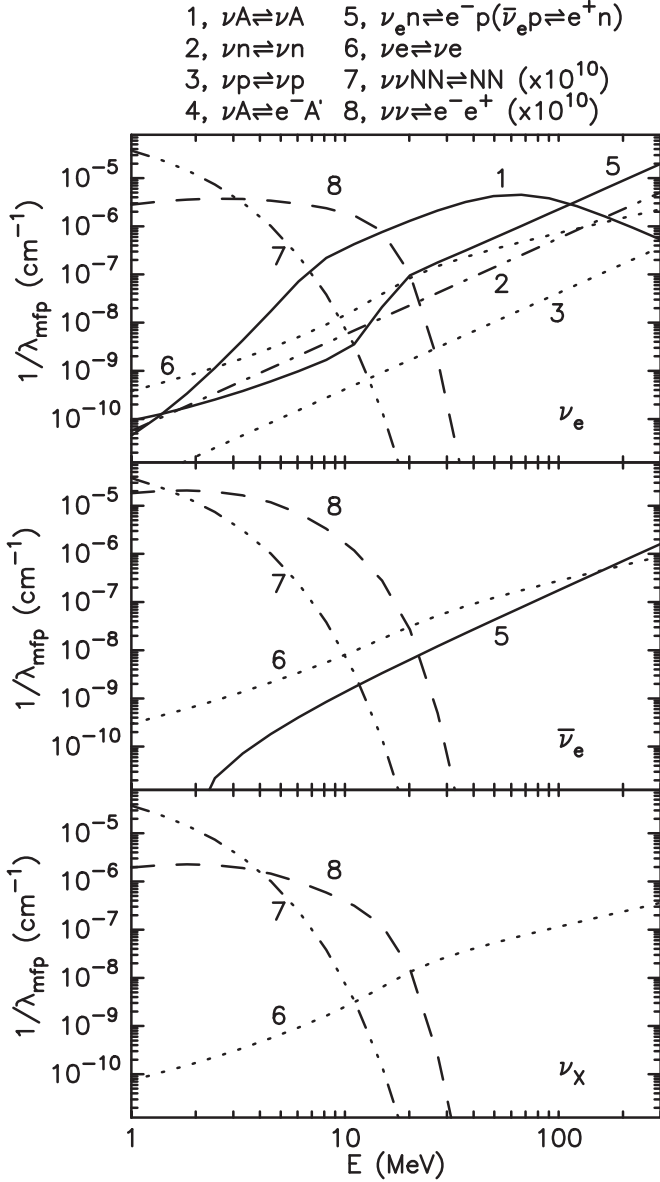


Figure 18. Same as Figure 17 but with $\rho = 10^{11} \text{ g cm}^{-3}$, $T = 1.382 \text{ MeV}$, and $Y_e = 0.4$. This hydrodynamical profile returns $s = 1.19 k_B \text{ baryon}^{-1}$, $A = 73.9$, and $Z = 30.5$. Since $N = A - Z > 40$, neutrino absorption on heavy nuclei is blocked with our current electron capture rate (Equation (90)).

terms. To expel the ambiguities coming from the spatial advection term, we develop a new spherically symmetric M1 code in the Newtonian limit. The basis of the new 1D code is the same as our main 3D Cartesian grid-based code. We solve Equation (32) with the same neutrino opacities used in model “s15Nso_1d.b” in Buras et al. (2006b). The spatial advection term $S_{\text{adv},s}$ in 1D spherical symmetry is evaluated in a similar way as in Nakamura et al. (2014b) and Horiuchi et al. (2014) and the advection terms in energy space $S_{\text{adv},e}$ are also slightly modified for the spherical polar coordinate. To take the same approach as the recent M1 neutrino transport codes (O’Connor 2014; Just et al. 2015), we solve the advection terms in energy space $S_{\text{adv},e}$ explicitly in time.

In Figure 20, we plot our results (1D–Sph) for the neutrino luminosity, mean energy, shock radius, and the Y_e profile together with reference values of VERTEX-PROMETHEUS (model “s15Nso_1d.b” in Buras et al. 2006b; VX–N15)

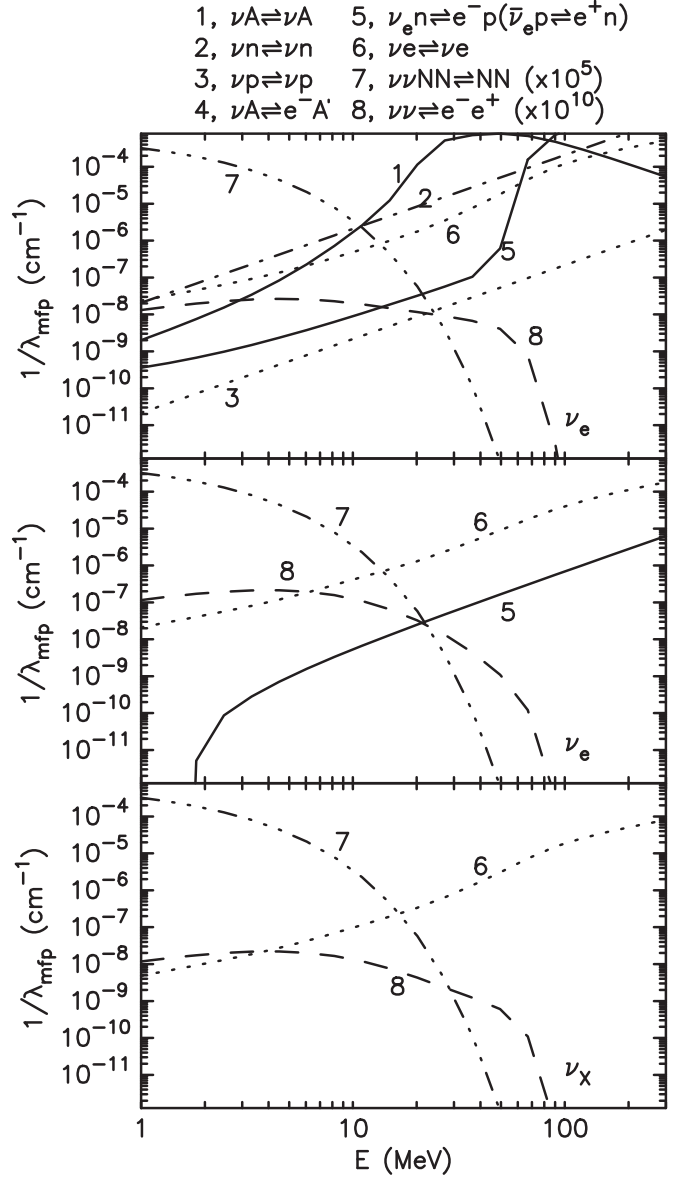


Figure 19. Same as Figure 17 but with $\rho = 10^{13} \text{ g cm}^{-3}$, $T = 3 \text{ MeV}$, and $Y_e = 0.25$. This hydrodynamical profile returns $s = 1.25 k_B \text{ baryon}^{-1}$, $A = 167.7$, and $Z = 49.3$. Since $N = A - Z > 40$, neutrino absorption on heavy nuclei is blocked with our current electron capture rate (Equation (90)).

except the Y_e profile. In the Y_e profile, we also plot results obtained from a model with solving $S_{\text{adv},e}$ implicitly in time, i.e., as the same as our main 3D code. Our results show a good agreement with VX–N15. The maximum deviations are $\sim 7 \times 10^{51} \text{ erg s}^{-1}$ in the luminosity and $\sim 0.9 \text{ MeV}$ in the mean energy. The mean energies, $\langle \varepsilon_{\nu_e} \rangle$ and $\langle \varepsilon_{\bar{\nu}_e} \rangle$, show slightly higher values than the reference ones. They are, however, within the error bounds reported in previous code comparisons (Liebendörfer et al. 2005; Müller et al. 2010). The neutrino luminosities show quite consistent behavior, especially in late phase $T_{\text{pb}} \gtrsim 150 \text{ ms}$, when the neutrino heating becomes more important. Contrary to our main results reported in Section 5.2, the Y_e trough observed at $R \sim 10^6 \text{ cm}$ (see Figure 13) disappears in the explicit model (solid lines), while the Y_e trough still exists in the implicit model (dotted). These two models support the idea to evaluate both $S_{\text{adv},s}$ and $S_{\text{adv},e}$ at the same time slice. We are going to examine this point in our main

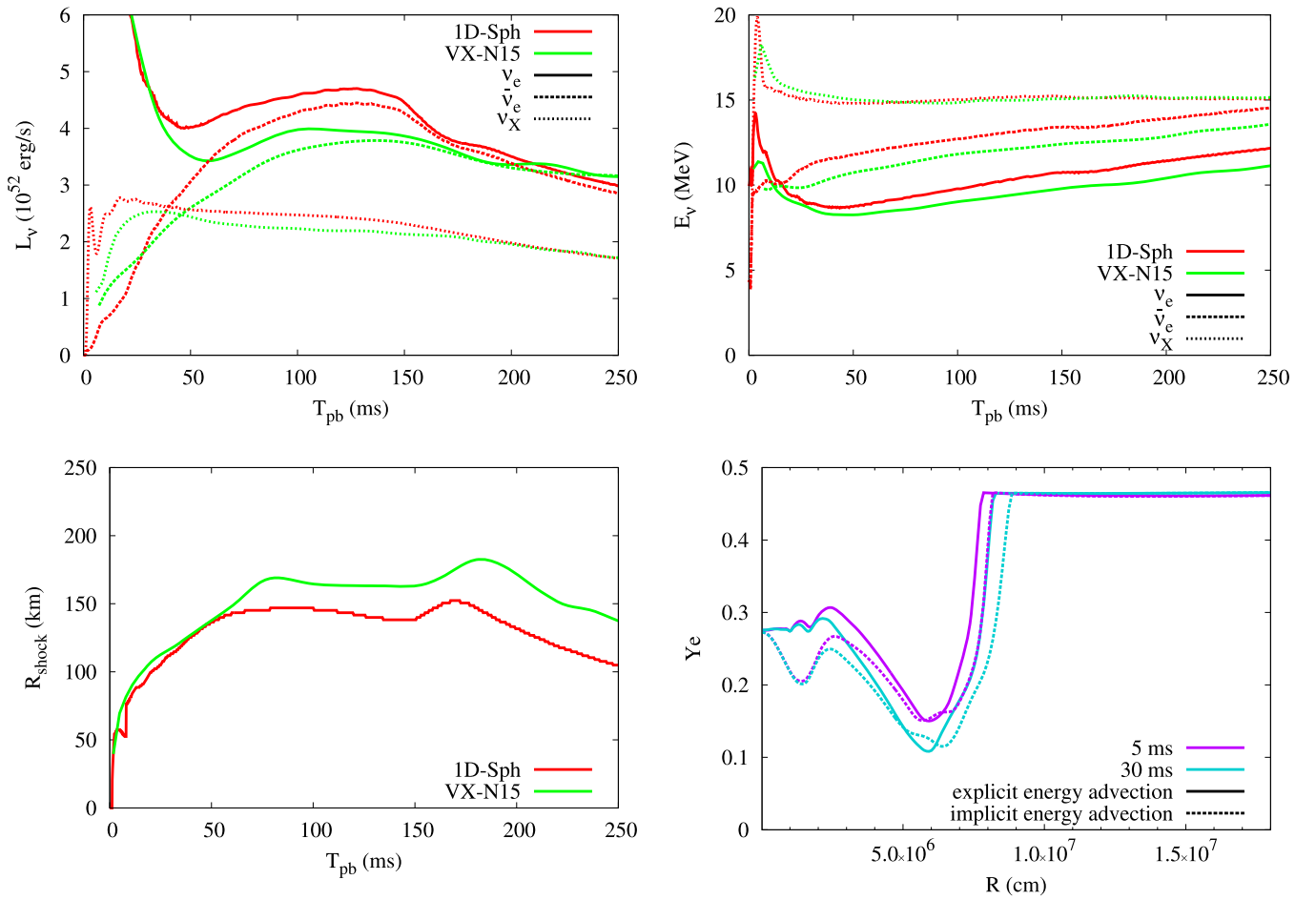


Figure 20. Top left panel: time evolution of the neutrino luminosities measured at 400 km. Results for our 1D spherical M1 transport scheme (1D–Sph) and for VERTEX-PROMETHEUS (VX–N15) are denoted by red and green lines, respectively. Top right: same as the top left one but for the mean neutrino energies. Bottom left: time evolution of the shock radius. Bottom right: radial profile of the electron fraction Y_e at different time slices. Solid and dotted lines are for the explicit and implicit models, respectively.

3D Cartesian based code in the near future. From this test, we confirm that the neutrino matter interaction terms are correctly implemented.

REFERENCES

- Ardeljan, N. V., Bisnovatyi-Kogan, G. S., & Moiseenko, S. G. 2000, *A&A*, **355**, 1181
- Audit, E., Charrier, P., Chièze, J., & Dubroca, B. 2002, *astro-ph*
- Bartl, A., Pethick, C. J., & Schwenk, A. 2014, *PhRvL*, **113**, 081101
- Baumgart, T. W., & Shapiro, S. L. 1999, *PhRvD*, **59**, 024007
- Bethe, H. A. 1990, *RvMP*, **62**, 801
- Bethe, H. A., & Wilson, J. R. 1985, *ApJ*, **295**, 14
- Blondin, J. M., & Mezzacappa, A. 2007, *Natur*, **445**, 58
- Blondin, J. M., Mezzacappa, A., & DeMarino, C. 2003, *ApJ*, **584**, 971
- Brandt, T. D., Burrows, A., Ott, C. D., & Livne, E. 2011, *ApJ*, **728**, 8
- Bruenn, S. W. 1985, *ApJS*, **58**, 771
- Bruenn, S. W., De Nisco, K. R., & Mezzacappa, A. 2001, *ApJ*, **560**, 326
- Bruenn, S. W., & Haxton, W. C. 1991, *ApJ*, **376**, 678
- Bruenn, S. W., & Mezzacappa, A. 1997, *PhRvD*, **56**, 7529
- Bruenn, S. W., Mezzacappa, A., Hix, W. R., et al. 2009, *JPhCS*, **180**, 012018
- Bruenn, S. W., Mezzacappa, A., Hix, W. R., et al. 2013, *ApJL*, **767**, L6
- Buras, R., Janka, H.-T., Rampp, M., & Kifonidis, K. 2006a, *A&A*, **457**, 281
- Buras, R., Rampp, M., Janka, H.-T., & Kifonidis, K. 2006b, *A&A*, **447**, 1049
- Burrows, A. 2013, *RvMP*, **85**, 245
- Burrows, A., Dessart, L., Livne, E., Ott, C. D., & Murphy, J. 2007, *ApJ*, **664**, 416
- Burrows, A., Hayes, J., & Fryxell, B. A. 1995, *ApJ*, **450**, 830
- Burrows, A., Reddy, S., & Thompson, T. A. 2006, *NuPhA*, **777**, 356
- Cardall, C. Y., Endeve, E., & Mezzacappa, A. 2013a, *PhRvD*, **88**, 023011
- Cardall, C. Y., Endeve, E., & Mezzacappa, A. 2013b, *PhRvD*, **87**, 103004
- Cernohorsky, J., & Bludman, S. A. 1994, *ApJ*, **433**, 250
- Couch, S. M. 2013, *ApJ*, **775**, 35
- Couch, S. M., & Ott, C. D. 2013, *ApJL*, **778**, L7
- Dimmelmeier, H., Font, J. A., & Müller, E. 2002, *A&A*, **388**, 917
- Fernández, R., Müller, B., Foglizzo, T., & Janka, H.-T. 2014, *MNRAS*, **440**, 2763
- Fernández, R., & Thompson, C. 2009, *ApJ*, **697**, 1827
- Fischer, T., Langanke, K., & Martínez-Pinedo, G. 2013, *PhRvC*, **88**, 065804
- Foglizzo, T., Galletti, P., Scheck, L., & Janka, H.-T. 2007, *ApJ*, **654**, 1006
- Foglizzo, T., Kazeroni, R., Guilet, J., et al. 2015, *PASA*, **32**, 9
- Foglizzo, T., Masset, F., Guilet, J., & Durand, G. 2012, *PhRvL*, **108**, 051103
- Foglizzo, T., Scheck, L., & Janka, H.-T. 2006, *ApJ*, **652**, 1436
- Fryer, C., Benz, W., Herant, M., & Colgate, S. A. 1999, *ApJ*, **516**, 892
- Guilet, J., & Foglizzo, T. 2012, *MNRAS*, **421**, 546
- Hanke, F., Marek, A., Müller, B., & Janka, H.-T. 2012, *ApJ*, **755**, 138
- Hanke, F., Müller, B., Wongwathanarat, A., Marek, A., & Janka, H.-T. 2013, *ApJ*, **770**, 66
- Hannestad, S., & Raffelt, G. 1998, *ApJ*, **507**, 339
- Harten, A., Lax, P. D., & Leer, B. v. 1983, *SIAMR*, **25**, 35
- Herant, M., Benz, W., Hix, W. R., Fryer, C. L., & Colgate, S. A. 1994, *ApJ*, **435**, 339
- Horiuchi, S., Nakamura, K., Takiwaki, T., Kotake, K., & Tanaka, M. 2014, *MNRAS*, **445**, L99
- Horowitz, C. J. 2002, *PhRvD*, **65**, 043001
- Iwakami, W., Kotake, K., Ohnishi, N., Yamada, S., & Sawada, K. 2008, *ApJ*, **678**, 1207
- Iwakami, W., Kotake, K., Ohnishi, N., Yamada, S., & Sawada, K. 2009, *ApJ*, **700**, 232
- Iwakami, W., Nagakura, H., & Yamada, S. 2014, *ApJ*, **793**, 5
- Janka, H.-T. 1992, *A&A*, **256**, 452

- Janka, H.-T. 2012, *ARNPS*, **62**, 407
- Janka, H.-T., & Müller, E. 1996, *A&A*, **306**, 167
- Juodagalvis, A., Langanke, K., Hix, W. R., Martínez-Pinedo, G., & Sampaio, J. M. 2010, *NuPhA*, **848**, 454
- Just, O., Obergaulinger, M., & Janka, H.-T. 2015, *MNRAS*, **453**, 3386
- Kanno, Y., Harada, T., & Hanawa, T. 2013, *PASJ*, **65**, 72
- Kitaura, F. S., Janka, H.-T., & Hillebrandt, W. 2006, *A&A*, **450**, 345
- Kotake, K. 2013, *CRPhy*, **14**, 318
- Kotake, K., Ohnishi, N., Yamada, S., & Sato, K. 2006a, *JPhCS*, **31**, 95
- Kotake, K., Sato, K., & Takahashi, K. 2006b, *RPPH*, **69**, 971
- Kotake, K., Sawai, H., Yamada, S., & Sato, K. 2004, *ApJ*, **608**, 391
- Kotake, K., Sumiyoshi, K., Yamada, S., et al. 2012a, *PTEP*, **2012**, 010000
- Kotake, K., Takiwaki, T., Suwa, Y., et al. 2012b, *AdAst*, **2012**, 428757
- Kotake, K., Yamada, S., & Sato, K. 2003, *PhRvD*, **68**, 044023
- Kuroda, T., Kotake, K., & Takiwaki, T. 2012, *ApJ*, **755**, 11
- Kuroda, T., Takiwaki, T., & Kotake, K. 2014, *PhRvD*, **89**, 044011
- Kuroda, T., & Umeda, H. 2010, *ApJS*, **191**, 439
- Langanke, K., & Martínez-Pinedo, G. 2000, *NuPhA*, **673**, 481
- Langanke, K., Martínez-Pinedo, G., Sampaio, J. M., et al. 2003, *PhRvL*, **90**, 241102
- Lattimer, J. M., & Douglas Swesty, F. 1991, *NuPhA*, **535**, 331
- Lentz, E. J., Mezzacappa, A., Bronson Messer, O. E., Hix, W. R., & Bruenn, S. W. 2012a, *ApJ*, **760**, 94
- Lentz, E. J., Mezzacappa, A., Bronson Messer, O. E., et al. 2012b, *ApJ*, **747**, 73
- Levermore, C. D. 1984, *QSRRT*, **31**, 149
- Liebendörfer, M., Messer, O. E. B., Mezzacappa, A., et al. 2004, *ApJS*, **150**, 263
- Liebendörfer, M., Mezzacappa, A., Thielemann, F.-K., et al. 2001, *PhRvD*, **63**, 103004
- Liebendörfer, M., Rampp, M., Janka, H.-T., & Mezzacappa, A. 2005, *ApJ*, **620**, 840
- Liebendörfer, M., Whitehouse, S. C., & Fischer, T. 2009, *ApJ*, **698**, 1174
- Livne, E., Burrows, A., Walder, R., Lichtenstadt, I., & Thompson, T. A. 2004, *ApJ*, **609**, 277
- Marek, A., Dimmelmeier, H., Janka, H.-T., Müller, E., & Buras, R. 2006, *A&A*, **445**, 273
- Marek, A., & Janka, H.-T. 2009, *ApJ*, **694**, 664
- Martínez-Pinedo, G., Fischer, T., Lohs, A., & Huther, L. 2012, *PhRvL*, **109**, 251104
- Masada, Y., Takiwaki, T., & Kotake, K. 2015, *ApJL*, **798**, L22
- Masada, Y., Takiwaki, T., Kotake, K., & Sano, T. 2012, *ApJ*, **759**, 110
- May, M. M., & White, R. H. 1966, *PhRv*, **141**, 1232
- Meakin, C. A., Sukhbold, T., & Arnett, W. D. 2011, *Ap&SS*, **336**, 123
- Melson, T., Janka, H.-T., & Marek, A. 2015, *ApJL*, **801**, L24
- Mezzacappa, A., & Bruenn, S. W. 1993a, *ApJ*, **405**, 669
- Mezzacappa, A., & Bruenn, S. W. 1993b, *ApJ*, **410**, 740
- Mezzacappa, A., & Bruenn, S. W. 1993c, *ApJ*, **405**, 637
- Mezzacappa, A., Bruenn, S. W., Lentz, E. J., et al. 2014, in *ASP Conf. Ser.* 488, 8th Int. Conf. of Numerical Modeling of Space Plasma Flows (ASTRONUM 2013), ed. N. V. Pogorelov, E. Audit, & G. P. Zank (San Francisco, CA: ASP), 102
- Mezzacappa, A., & Matzner, R. A. 1989, *ApJ*, **343**, 853
- Minerbo, G. N. 1978, *QSRRT*, **20**, 541
- Mösta, P., Richers, S., Ott, C. D., et al. 2014, *ApJL*, **785**, L29
- Müller, E., & Janka, H.-T. 1997, *A&A*, **317**, 140
- Müller, B., & Janka, H.-T. 2014, *ApJ*, **788**, 82
- Müller, B., & Janka, H.-T. 2015, *MNRAS*, **448**, 2141
- Müller, B., Janka, H.-T., & Dimmelmeier, H. 2010, *ApJS*, **189**, 104
- Müller, B., Janka, H.-T., & Heger, A. 2012a, *ApJ*, **761**, 72
- Müller, B., Janka, H.-T., & Marek, A. 2012b, *ApJ*, **756**, 84
- Murphy, J. W., & Burrows, A. 2008, *ApJ*, **688**, 1159
- Nagakura, H., Sumiyoshi, K., & Yamada, S. 2014, *ApJS*, **214**, 16
- Nakamura, K., Kuroda, T., Takiwaki, T., & Kotake, K. 2014a, *ApJ*, **793**, 45
- Nakamura, K., Takiwaki, T., Kuroda, T., & Kotake, K. 2014b, arXiv
- Obergaulinger, M., Aloy, M. A., Dimmelmeier, H., & Müller, E. 2006, *A&A*, **457**, 209
- Obergaulinger, M., & Janka, H.-T. 2011, arXiv:1101.1198
- Obergaulinger, M., Janka, H.-T., & Aloy, M. A. 2014, *MNRAS*, **445**, 3169
- O'Connor, E. 2015, *ApJS*, **219**, 24
- O'Connor, E., & Ott, C. D. 2011, *ApJ*, **730**, 70
- O'Connor, E., & Ott, C. D. 2013, *ApJ*, **762**, 126
- Ohnishi, N., Kotake, K., & Yamada, S. 2006, *ApJ*, **641**, 1018
- Ott, C. D., Abdikamalov, E., O'Connor, E., et al. 2012, *PhRvD*, **86**, 024026
- Ott, C. D., Burrows, A., Dessart, L., & Livne, E. 2008, *ApJ*, **685**, 1069
- Perego, A., Gafton, E., Cabezón, R., Rosswog, S., & Liebendörfer, M. 2014, *A&A*, **568**, A11
- Peres, B., Penner, A. J., Novak, J., & Bonazzola, S. 2014, *CQGra*, **31**, 045012
- Pomraning, G. C. 1981, *QSRRT*, **26**, 385
- Pons, J. A., Ibáñez, J. M., & Miralles, J. A. 2000, *MNRAS*, **317**, 550
- Rampp, M., & Janka, H.-T. 2002, *A&A*, **396**, 361
- Rosswog, S., & Liebendörfer, M. 2003, *MNRAS*, **342**, 673
- Ruffert, M., Janka, H.-T., & Schaefer, G. 1996, *A&A*, **311**, 532
- Sanchis-Gual, N., Montero, P. J., Font, J. A., Müller, E., & Baumgarte, T. W. 2014, *PhRvD*, **89**, 104033
- Sato, K. 1975, *PThPh*, **54**, 1325
- Sawai, H., Yamada, S., & Suzuki, H. 2013, *ApJL*, **770**, L19
- Scheck, L., Kifonidis, K., Janka, H., & Müller, E. 2006, *A&A*, **457**, 963
- Scheidegger, S., Käppeli, R., Whitehouse, S. C., Fischer, T., & Liebendörfer, M. 2010, *A&A*, **514**, A51
- Schwartz, R. A. 1967, *AnPhy*, **43**, 42
- Sekiguchi, Y. 2010, *PThPh*, **124**, 331
- Shibata, M., Kiuchi, K., Sekiguchi, Y., & Suwa, Y. 2011, *PThPh*, **125**, 1255
- Shibata, M., Nagakura, H., Sekiguchi, Y., & Yamada, S. 2014, *PhRvD*, **89**, 084073
- Shibata, M., & Nakamura, T. 1995, *PhRvD*, **52**, 5428
- Shibata, M., & Sekiguchi, Y.-I. 2004, *PhRvD*, **69**, 084024
- Shibata, M., & Sekiguchi, Y.-I. 2005, *PhRvD*, **71**, 024014
- Skinner, M. A., & Ostriker, E. C. 2013, *ApJS*, **206**, 21
- Sumiyoshi, K., & Röpke, G. 2008, *PhRvC*, **77**, 055804
- Sumiyoshi, K., Takiwaki, T., Matsufuru, H., & Yamada, S. 2015, *ApJS*, **216**, 5
- Sumiyoshi, K., & Yamada, S. 2012, *ApJS*, **199**, 17
- Sumiyoshi, K., Yamada, S., Suzuki, H., et al. 2005, *ApJ*, **629**, 922
- Suwa, Y., Kotake, K., Takiwaki, T., Liebendörfer, M., & Sato, K. 2011, *ApJ*, **738**, 165
- Suwa, Y., Kotake, K., Takiwaki, T., et al. 2010, *PASJ*, **62**, L49
- Suwa, Y., Takiwaki, T., Kotake, K., et al. 2013, *ApJ*, **764**, 99
- Suwa, Y., Yamada, S., Takiwaki, T., & Kotake, K. 2016, *ApJ*, **816**, 43
- Swesty, F. D., & Myra, E. S. 2009, *ApJS*, **181**, 1
- Takiwaki, T., Kotake, K., & Suwa, Y. 2012, *ApJ*, **749**, 98
- Takiwaki, T., Kotake, K., & Suwa, Y. 2014, *ApJ*, **786**, 83
- Thompson, T. A., Burrows, A., & Pinto, P. A. 2003, *ApJ*, **592**, 434
- Thorne, K. S. 1981, *MNRAS*, **194**, 439
- Wilson, J. R. 1985, in *Numerical Astrophysics*, ed. J. M. Centrella, J. M. Leblanc, & R. L. Bowers, 422
- Woosley, S. E., & Bloom, J. S. 2006, *ARA&A*, **44**, 507
- Woosley, S. E., & Weaver, T. A. 1995, *ApJS*, **101**, 181
- Yamada, S. 1997, *ApJ*, **475**, 720
- Yamada, S., Janka, H.-T., & Suzuki, H. 1999, *A&A*, **344**, 533
- Yueh, W. R., & Buchler, J. R. 1976, *Ap&SS*, **41**, 221
- Zhang, W., Howell, L., Almgren, A., et al. 2013, *ApJS*, **204**, 7